

# Pressure–temperature–time evolution of subducted crust revealed by complex garnet zoning (Theodul Glacier Unit, Switzerland)

Thomas Bovay<sup>1</sup>  | Pierre Lanari<sup>1</sup>  | Daniela Rubatto<sup>1,2</sup>  | Matthijs Smit<sup>3</sup> | Francesca Piccoli<sup>1</sup>

<sup>1</sup>Institute of Geological Sciences, University of Bern, Bern, Switzerland

<sup>2</sup>Institut des Sciences de la Terre, University of Lausanne, Lausanne, Switzerland

<sup>3</sup>Department of Earth, Ocean and Atmospheric Sciences, University of British Columbia, Vancouver, BC, Canada

## Correspondence

Thomas Bovay, Institute of Geological Sciences, University of Bern, 3012 Bern, Switzerland.

Email: thomas.bovay@gmail.com

## Funding information

Schweizerischer Nationalfonds zur Förderung der Wissenschaftlichen Forschung, Grant/Award Number: Project N. 200021\_166280 and Project N. 206021\_170722

**Handling Editor:** Julia Baldwin

## Abstract

Collisional orogens commonly include mono-metamorphic and poly-metamorphic units, and their different evolution can be difficult to recognize and reconcile. The Theodul Glacier Unit (TGU) in the Western Alps consists of an association of meta-sedimentary and metamafic rocks embedded within the Zermatt-Saas tectonic unit. In spite of recent petrological studies, it remains unclear whether these rocks underwent one or multiple metamorphic cycles. In this study, different lithologies from the TGU unit (mafic schist, mafic granofels, and chloritoid schist) were investigated for petrography, quantitative compositional mapping of garnet, thermodynamic modelling, and Lu–Hf garnet dating. The data reveal a coherent mono-metamorphic history with a  $\beta$ -shaped pressure–temperature ( $P$ – $T$ ) path characteristic of oceanic subduction. Garnet Lu–Hf ages yield a restricted garnet crystallization time window between 50.3 and 48.8 Ma ( $\pm 0.5\%$ , 2SD). A prograde metamorphic stage recorded in garnet cores yields conditions of  $490 \pm 15^\circ\text{C}$  and  $1.75 \pm 0.05$  GPa. Maximum pressure conditions of  $2.65 \pm 0.10$  GPa and  $580 \pm 15^\circ\text{C}$  were reached at  $50.3 \pm 0.3$  Ma. Initial exhumation was rapid and led to isothermal decompression to  $1.50 \pm 0.10$  GPa within 1 Ma. This decompression was associated with lawsonite breakdown in mafic schist and in mafic granofels, causing intense fluid–rock interaction within and between different lithologies. This process is recorded in garnet textures and trace element patterns, and in the major element composition of K-white mica. Initial exhumation was followed by re-heating of  $\sim 30^\circ\text{C}$  at a pressure of  $1.50 \pm 0.10$  GPa. Perturbation of the subduction-zone thermal structure may be related to upwelling of hot asthenospheric mantle material and transient storage of the unit at the crust–mantle boundary.

## KEYWORDS

Lu–Hf garnet whole-rock geochronology, phase equilibria, quantitative compositional mapping, Zermatt-Saas Unit, Zr-in-rutile thermometry

This is an open access article under the terms of the Creative Commons Attribution-NonCommercial License, which permits use, distribution and reproduction in any medium, provided the original work is properly cited and is not used for commercial purposes.

© 2021 The Authors. *Journal of Metamorphic Geology* published by John Wiley & Sons Ltd.

## 1 | INTRODUCTION

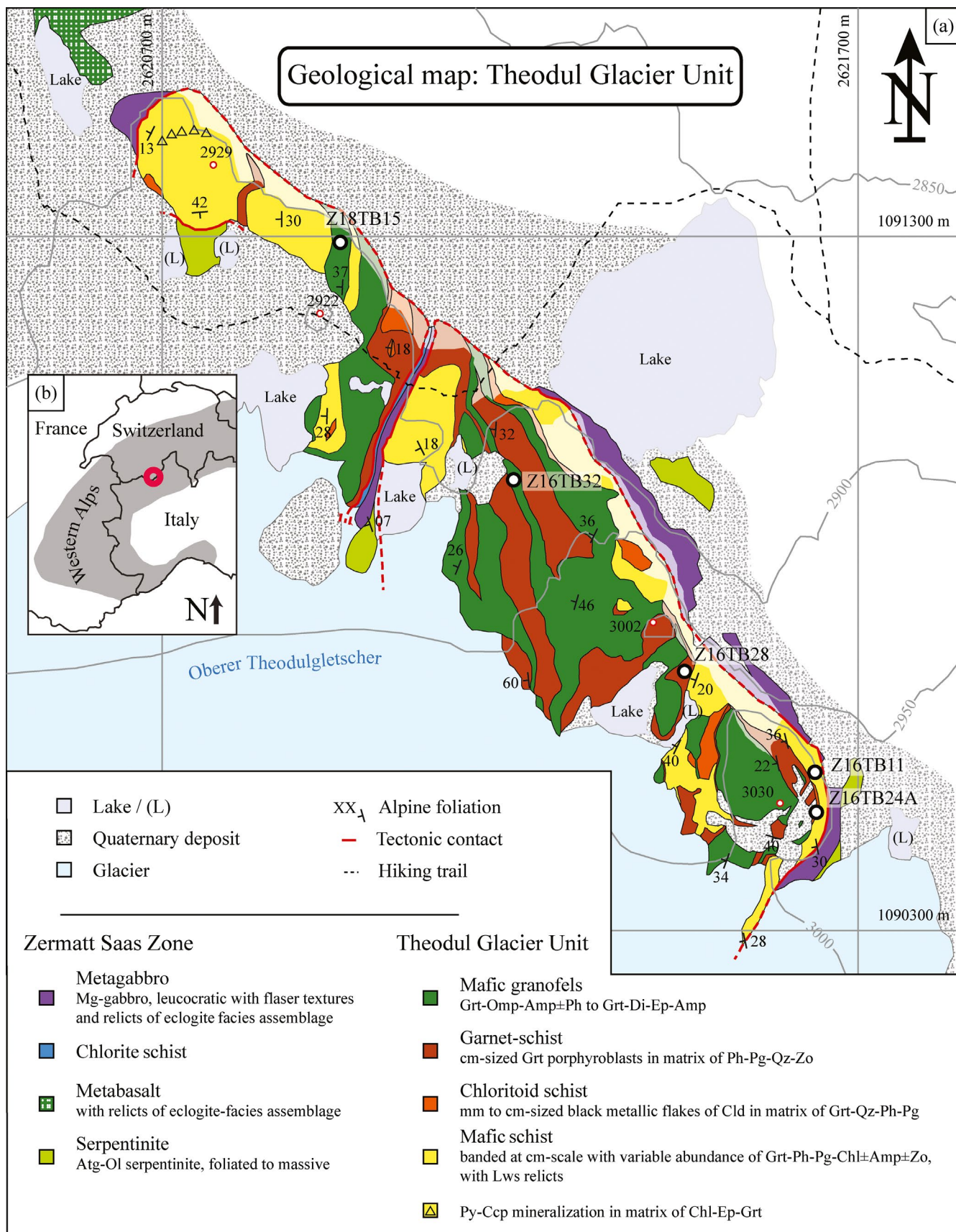
In poly-metamorphism terranes, several metamorphic cycles are experienced by a rock and each metamorphic cycle involves a sequence of prograde and retrograde transformations affecting the rock texture and mineral compositions. However, the transformation is rarely complete and mineral relics are key to decipher multi-stage events as well as pressure and temperature ( $P$ – $T$ ) evolution. Garnet is a common rock-forming mineral known to be resilient to re-equilibration (Baxter et al., 2013) and therefore is a good recorder of poly-metamorphism (Angiboust et al., 2017; Feenstra et al., 2007; Giuntoli et al., 2018; Lanari et al., 2017; Putnis, 2009; Thiessen et al., 2019). The study of garnet texture and chemical composition gives insights into its growth history. When temperatures are low enough to prevent intracrystalline diffusion, continuous garnet growth over a  $P$ – $T$  segment produces a typical chemical zoning witnessing local equilibrium between the garnet crystal and the matrix of the rock at the time of garnet growth (Spear, 1988). For example, Mn strongly partitions into garnet and spessartine is consequently enriched in the core relative to the rim composition and exhibits a bell-shape zoning pattern (Hollister, 1966). On the other hand, a sharp compositional contact between distinct garnet zones within a single crystal is commonly interpreted as reflecting two distinct metamorphic stages or metamorphic cycles (Compagnoni, 1977; Giuntoli, Lanari, Burn, et al., 2018; Le Bayon & Ballèvre, 2004; Manzotti & Ballèvre, 2013), or as a consequence of the infiltration of externally derived fluids (e.g. Angiboust et al., 2014; Jamtveit & Hervig, 1994). Garnet major element composition is additionally influenced by the reactive bulk composition, which is the bulk composition of the reactive volume (e.g. Lanari & Engi, 2017). The reactive bulk composition changes during garnet growth by fractionation (Evans, 2004; Konrad-Schmolke et al., 2011) affecting the isopleth positions in equilibrium phase diagrams (Lanari & Engi, 2017; Spear, 1988). In addition, the same garnet composition can be predicted to be stable under different geotherms (e.g. at High- $T$ –Low- $P$  and Low- $T$ –High- $P$ ) for a given bulk composition (see figure 8 in Lanari & Engi, 2017). This will inevitably complicate the interpretation of garnet zoning and the distinction between mono- and poly-metamorphic growth.

Besides its chemistry, garnet geochronology enables time constraints, providing a further key tool to distinguish between mono- and poly-metamorphic growth. Both Lu–Hf and Sm–Nd systematics can be employed as chronometers in garnet, because for both systems garnet solely fractionates parent over daughter forming an unusually high parent/daughter isotope ratio (Baxter et al., 2017). The main advantage of Lu–Hf geochronology is that the diffusivity of Hf is low with respect to Nd, making Lu–Hf systematics less susceptible to be affected by diffusive isotope re-equilibration

(Bloch et al., 2015; Kohn, 2009; Scherer et al., 2000; Smit et al., 2013). During garnet growth, Lu is generally enriched in the garnet core due to the high compatibility of Lu in garnet (e.g. Konrad-Schmolke, O'Brien, et al., 2008). As a consequence, Lu–Hf ages of bulk garnet crystals are typically biased towards the initial stage of garnet growth (Konrad-Schmolke, O'Brien, et al., 2008; Lapen et al., 2003; Otamendi et al., 2002; Skora et al., 2006). However, complex Lu zoning in garnet is sometimes observed, where distinct garnet zones are enriched in Lu. Such element distribution might increase the complexity of age interpretation, especially if garnet growth duration between Lu maxima exceeds analytical precision (Lapen et al., 2003; Skora et al., 2006; Smit et al., 2010).

In the Western Alps, the recognition of, and distinction between, mono- and polycyclic metamorphic terranes has become of crucial importance in tectonic and palaeogeographic reconstructions. Mono-metamorphic units are clearly present in the form of terranes comprising Mesozoic sediments and Jurassic–Cretaceous oceanic crust metamorphosed during the Alpine orogeny (e.g. Zermatt-Saas Zone, ZSZ). Poly-metamorphic units are found or suspected in various locations. These are interpreted as portions of continental basement which, in addition to their Alpine overprint, record Permian, and/or older metamorphism (e.g. the Sesia Zone and Dent Blanche; Manzotti et al., 2014). An example of a unit that is potentially poly-metamorphic, yet not fully identified as such, is the Theodul Glacier Unit (TGU)—a metasedimentary sliver embedded within the ZSZ (Figure 1) that has been described as a coherent unit (Weber & Bucher, 2015). This unit largely preserves an Alpine, high- $P$  assemblage, but was recently interpreted as poly-metamorphic, based on the investigation of garnet textures and thermodynamic modelling (Bucher et al., 2019, 2020). The TGU has been therefore interpreted as a small continental outlier embedded in the oceanic units of the ZSZ. Alternatively, the unit could be mono-metamorphic, representing a sedimentary sequence deposited on the oceanic crust of the ZSZ ophiolite, much alike the metasediments of the Lago di Cignana locality (Reinecke, 1998).

To better constrain the metamorphic history and tectonic significance of the TGU, various rocks from this unit were subjected to a multi-method analysis. Two potentially poly-metamorphic metasedimentary lithologies were studied and their results compared with those from metamafic rocks, with the latter being used as benchmark to characterize the mono-metamorphic character of the  $P$ – $T$  path of this unit. The mono- versus poly-metamorphic character of garnet in the metasedimentary rocks was assessed based on petrological observations, quantitative compositional mapping, thermodynamic modelling, and Lu–Hf chronology. Additional compositional mapping and thermodynamic modelling was performed on phengite. Zr-in-rutile content and chloritoid



stability were used to constrain temperature conditions at specific metamorphic stage. Our results show that the TGU is a mono-metamorphic unit that followed a  $\beta$ -shaped  $P$ – $T$  path during the Eocene Alpine metamorphic cycle.

## 2 | GEOLOGICAL AND TECTONIC SETTINGS

The Penninic domain in the Western Alps is a complexly folded nappe stack of rocks with continental and oceanic origin that have different metamorphic histories and were assembled during the Alpine orogeny. The ZSZ is a south Penninic tectonic unit made of Mesozoic ophiolites that underwent UHP and eclogitic HP metamorphism (Beaith, 1967; Dal Piaz & Ernst, 1978; Reinecke, 1991) during Eocene (Amato et al., 1999; De Meyer et al., 2014; Duchêne et al., 1997; Lapen et al., 2003; Rubatto et al., 1998). It has been interpreted as being an exhumed relict of the Piemont–Ligurian oceanic lithosphere with mid-ocean ridge affinity (Beaith, 1967), which is now sandwiched between the underlying Briançonnais basement (e.g. the Monte Rosa and the Gran Paradiso massifs) and the overlying Austroalpine units (e.g. the Sesia–Dent Blanche nappe system; Escher et al., 1997). The ZSZ is made of an association of ultramafic rocks, mafic rocks, and metasediments, representing a dismembered ophiolitic sequence (Beaith, 1967). Whether the ZSZ is a coherent piece of oceanic lithosphere, which was then only partially disrupted during exhumation (Angiboust et al., 2009), or whether it is a tectonic mélange of different tectonic slices (Bousquet et al., 2008; Groppo et al., 2009; Negro et al., 2013) is still unclear.

The ophiolites of the ZSZ consist of metamorphosed metabasalts and metagabbros of Jurassic protolith age (Beltrando et al., 2010; Pleuger et al., 2007; Rubatto et al., 1998; Rubatto & Hermann, 2003) situated on top of a thick section of serpentinite (Fassmer et al., 2016; Kirst & Leiss, 2016; Pleuger et al., 2007). The oceanic sedimentary cover—also referred to as *Schistes Lustrés* or *Bündnerschiefer*—is mainly composed of marbles, schists, calcareous schists, meta-radiolarites, and Mn-bearing meta-cherts with a Jurassic to Cretaceous protolith age (Beaith, 1967). The sediments that overlie the metabasalts and metagabbros form a thin continuous cover of the oceanic crust (Pal Piaz, 1979). The overall stratigraphy shows slow spreading ridge affinity (Dilek & Furnes, 2014).

Three kilometre-thick slices of continental crust that were reworked at high- $P$  conditions occur discontinuously throughout the ZSZ section, especially in its uppermost part: Etirol-Levaz, Glacier Rafray, and Monte Emilius. They are either localized within the ophiolitic nappe of the ZSZ (Angiboust et al., 2017; Ballèvre et al., 1986; Beltrando et al., 2010; Dal Piaz, 2001; Fassmer et al., 2016; Kirst & Leiss, 2016) or along the tectonic contact between the Combin zone and ZSZ

(Dal Piaz et al., 2001). Two different origins have been proposed for these continental slices: (a) They are slivers of one of the adjacent continental units, which were incorporated into the ZSZ during the Alpine orogeny (Kirst & Leiss, 2016; Pleuger et al., 2007). This interpretation explains the similarities with the typical characteristics of the Sesia-Zone and the Dent Blanche nappe (Pleuger et al., 2007). (b) They are fragments of continental crust that were dismembered during Permian to Jurassic extension to form extensional allochthons over the Mesozoic oceanic crust (Beltrando et al., 2010; Dal Piaz, 2001). In the latter case they would form a palaeogeographic entity with the ZSZ zone (Fassmer et al., 2016). A similar close relationship between continental basement slices and serpentinites is commonly found along ocean–continent transition zones, where movements along detachment faults dipping underneath the thinned continental margin result in the tectonic erosion of small pieces of the margin (Beltrando et al., 2010, 2014; Péron-Pinvidic & Manatschal, 2009; Vitale Brovarone et al., 2011).

The TGU is located SW of the village of Zermatt in Switzerland, close to the Trockener Steg cable car station. The outcropping rocks show little weathering as the retreat of the ‘Oberer Theodulgletscher’ occurred only during the last three decades. The TGU is an association of metasedimentary and metamafic rocks embedded within the ZSZ unit (Figure 1), which has been mapped as a coherent unit (Bovay, 2021; Weber & Bucher, 2015). The mafic rocks from TGU show within-Plate Basalt chemistry (Weber & Bucher, 2015). Thermodynamic modelling of the eclogitic rocks based on garnet chemistry suggests a mono-metamorphic history with a peak metamorphism at  $2.20 \pm 0.10$  GPa and  $580 \pm 50^\circ\text{C}$ , slightly lower than those of the ZSZ eclogites (Weber & Bucher, 2015). Garnet Lu–Hf dating of mafic rocks records prograde metamorphic mineral growth and yields an Alpine age at 58–56 Ma (Weber et al., 2015), which is slightly older than the peak metamorphism of ZSZ dated between 50 and 40 Ma (De Meyer et al., 2014; Dragovic et al., 2020; Duchêne et al., 1997; Lapen et al., 2003; Rubatto et al., 1998). On the other hand, zircon U–Pb dating yields an age of  $295 \pm 16$  Ma, which was interpreted to date pre-Alpine granulite facies metamorphism (Bucher et al., 2020). The metasedimentary rocks have been described as an association of garnet–phengite schists and garnet–biotite schists (Weber & Bucher, 2015). In this work, detailed field investigation (Figure 1) resulted in the subdivision of the garnet–phengite schist lithology into two lithological units: garnet schist and mafic schist. In addition, the garnet–biotite schists are renamed as chloritoid schist (Cld-schist), consistent with the observed mineral assemblage (see below). In summary, the highly foliated metasedimentary rocks consist of an intricate imbrication of mafic schist, garnet schist, and Cld-schist that constitute a coherent unit. Large garnet porphyroblasts in the garnet schist recorded two metamorphic stages: a pre-Alpine

granulitic core stable at  $\sim 0.7$  GPa and  $\sim 780^\circ\text{C}$  is overgrown by an Alpine rim generation formed at  $\sim 1.7$  GPa and  $\sim 530^\circ\text{C}$  (Bucher et al., 2019). Cation diffusion across the contact between the two garnet generations occurred at  $530\text{--}580^\circ\text{C}$  and relaxed zoning for *c.* 10 Ma (Bucher et al., 2019).

### 3 | PETROLOGICAL DESCRIPTION

To better constrain the *P*–*T* conditions experienced by the TGU, we performed a petrological study focusing on mafic granofels and metasedimentary schists. In this study, three types of lithologies are investigated: the mafic granofels, the mafic schist, and the Cld-schist.

#### 3.1 | Mafic granofels

Mafic granofels occur either as large bodies of 10 m wide and 10–100 m long, or as smaller, stretched boudins of various sizes (cm to m) embedded within the surrounding schists (Figure 2a). This variable lithology can be described by two characteristic types of mineral assemblage (Table 1) (Figure 2b,c). The first type of TGU mafic granofels (sample Z18TB15) has an assemblage of garnet–omphacite–amphibole±phengite (Figure 2b,d,e), similar to that described by Weber and Bucher (2015). The second rock type (sample Z16TB32) shows an assemblage of garnet, diopside, zoisite and/or zoisite–epidote solid solution, and amphibole (Figure 2c). Due to the highly variable mineral modal composition of the mafic rocks, in the field they range in colour from milky to dark green (Figure 2a–d). Garnet grains are mostly euhedral with diameters between 1 and 5 mm and may show textural equilibrium with the amphiboles (Figure 2e). Mafic boudins exhibit undeformed cross-cutting veinlets of garnet–diopside–amphibole–quartz–calcite and show a continuous layer of euhedral garnet at the contact with the host rock on both vein sides. Retrogression locally replaced the main HP mineral assemblage with chlorite, amphibole, epidote, paragonite, albite, and titanite. According to Weber and Bucher (2015), the chemical composition of the different population of amphiboles are either unzoned glaucophane porphyroblasts or Ca-amphibole with actinolitic core and barrositic–edenitic rim. Retrogressed domains in mafic granofels show abundant albite–epidote veins.

#### 3.2 | Mafic schist

A variety of mafic schists are found interlayered at the centimetre to metre scale. The layers are oriented parallel to the main foliation and the transition from one type to another can be either gradual (mm to cm) or sharp (Figure 2f). The

mineral assemblage common to every type of mafic schist is garnet–phengite–paragonite–quartz–chlorite (Figure 2g), with additional zoisite and amphibole (Table 1). Mineral abundance can vary considerably; for example, sample Z16TB11 comprises <1 vol.% of zoisite and 15% amphibole, whereas sample Z16TB28 contains 10%–35% zoisite and up to 5% amphibole. Pseudomorphs after lawsonite were observed in every type of mafic schist (Figure 2f). These occur as whitish diamond-shaped mineral aggregates of up to 1 cm and are composed of zoisite–quartz–paragonite, sometimes with small euhedral garnet. Three main garnet populations are observed in the mafic schists (Figure 2g). (a) Sub-euhedral grains in the mineral matrix, which are up to 200  $\mu\text{m}$  in diameter and are mostly inclusion free. These occur either as banding of millimetre to centimetre scale in which each grain is stretched along the main foliation, or as clusters. This garnet type preserves complex zoning with relict cores and a distinct chemical composition from the other garnet types (see below). (b) Euhedral grains of 0.2–0.7 mm in diameter; these matrix garnet do not contain relict cores. (c) Euhedral garnet of 1–7 mm in diameter, which are rich in inclusion of various minerals (zoisite, rutile, titanite, apatite, pyrite, amphibole, quartz, zircon, and white mica). Inclusion textures in garnet vary from sample to sample and indicate syn to post kinematic entrapment. Greenschist facies retrogression caused local growth of chlorite and amphibole rims around garnet, titanite rims around rutile, and production of minor poikilitic albite.

#### 3.3 | Chloritoid schist

This lithology was previously mapped by Weber and Bucher (2015) as garnet–biotite schists. Both in the field and in thin section, biotite was not identified. Instead, abundant chloritoid flakes were observed along the Alpine foliation, hence here the term Cld-schist is adopted. This lithology (sample Z16TB24A) is typified by black metallic flakes of chloritoid in a foliated matrix of garnet, quartz, phengite, and paragonite (Figure 2h,i, Table 1). Rare altered amphibole porphyroblasts and elongated rutile are also present. Garnet grains are euhedral with a diameter of 0.2–0.4 mm and occasionally show an atoll-shaped texture. The lithology contains garnet–chloritoid–quartz veins.

## 4 | ANALYTICAL METHODS

### 4.1 | Scanning electron microscope and electron micro probe

Sample imaging (backscattered electron mode) was performed using a scanning electron microscope (SEM) ZEISS

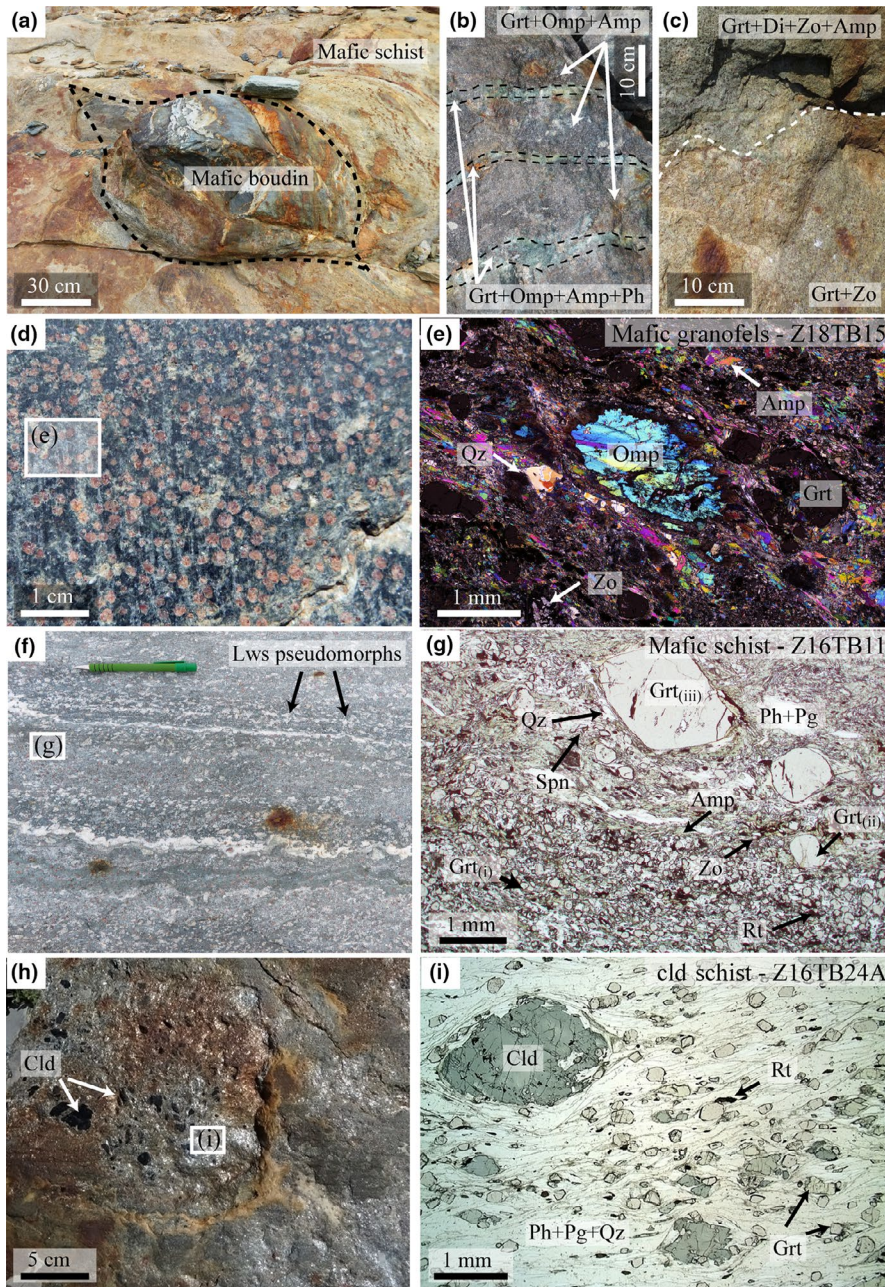


**FIGURE 2** Outcrop photographs and sample microphotographs from the representative lithologies of the TGU. Mineral abbreviations follow Whitney and Evans (2010). White squares in (d), (f), and (h) are representative location of indicated microphotograph. (a) Mafic boudin stretched within the schists. (b) Outcrop view of banded mafic granofels. (c) Outcrop view of mafic granofels with smooth transition between Di-rich to Zo-rich domain. (d) Outcrop view of mafic granofels: lighter areas are predominantly Omp-rich, whereas darker areas are Amp-rich. (e) Microphotograph of mafic granofels Z18TB15 showing textural equilibrium between Omp and Grt, both surrounded by Amp. (f) Outcrop view of mafic schist. Layering is parallel with the well-developed foliation. White diamonds-shaped domains are interpreted as pseudomorphs after lawsonite. (g) Scanned thin section of mafic schist Z16TB11 showing transition from a zone rich in small garnet (<200  $\mu\text{m}$ , bottom of image) to a zone richer in garnet porphyroblasts. (h) Outcrop view of a Cld-schist, with dark flaky chloritoid. (i) Scanned thin section image of Cld-schist Z16TB24A: the foliation is marked by Ph+Pg+Qz [Colour figure can be viewed at [wileyonlinelibrary.com](http://wileyonlinelibrary.com)]

EVO50 at the Institute of Geological Sciences (University of Bern) with 20 keV acceleration voltage and 1 nA beam current.

Quantitative chemical analyses of garnet, white mica, and chloritoid were performed with the electron probe microanalyser (EPMA) JEOL JXA-8200 superprobe at the Institute of Geological Science (University of Bern). Spot analyses were performed using 15 keV accelerating voltage, 20 nA specimen current, and 40 s dwell time (10 s for each background after 20 s on peak). Nine oxide components were obtained using synthetic and natural standards: almandine ( $\text{SiO}_2$ ,  $\text{Al}_2\text{O}_3$ , and  $\text{FeO}$ ), albite ( $\text{Na}_2\text{O}$ ), anorthite ( $\text{CaO}$ ), orthoclase ( $\text{K}_2\text{O}$ ), forsterite ( $\text{MgO}$ ), ilmenite ( $\text{TiO}_2$ ), and tephroite ( $\text{MnO}$ ).

Quantitative compositional maps were generated from X-ray intensity maps using spot analyses acquired in the same area as internal standards. The X-ray maps were measured by WDS with 15 keV accelerating voltage and 100 nA specimen current, with various dwell time and resolutions. Nine elements (Si, Ti, Al, Fe, Mn, Mg, Na, Ca, and K) were measured at the specific wavelength in two successive passes (with Na, Ca, and K analysed on the first scan). Compositional maps were processed using XMapTools 3.2.1 (Lanari et al., 2014, 2019). Structural formulas for garnet and phengite were calculated for each map using the external functions available in XMapTools and considering a minimum of 17 internal standards. Representative compositions of each garnet and phengite growth zone were obtained by averaging pixels

**TABLE 1** Sample list including geolocalization and mineral assemblages

Sample	Latitude	Longitude	Major phases	Minor phases
Mafic granofels				
Z16TB32	45°58'9.66"N	7°42'42.84"E	Grt+Ep+Di+Amp	Qz+Ttn+Ap
Z18TB15	45°58'20.9"N	7°42'34.8"E	Omp+Grt+Amp	Ep+Qz+Ph+Pg+Chl+Ap+Rt+Ttn
Mafic schist				
Z16TB11	45°58'1.04"N	7°43'0.53"E	Grt+Qz+Ph+Pg+Amp+Ep	Chl+Ab+Rt+Ttn+Ap
Z16TB28	45°58'1.26"N	7°42'56.64"E	Grt+Ep+Chl+Qz+Ph	Ttn+Rt+Ab+Ap
Chloritoid schist				
Z16TB24A	45°57'54.72"N	7°43'4.62"E	Grt+Qz+Ph+Pg+Clid+Amp	Chl+Rt+Ttn

from manually selected areas. The domains were chosen in a way to avoid any mixing between garnet and phengite generations, and excluding mineral inclusions.

## 4.2 | Bulk rock chemistry

Bulk rock chemical analyses were conducted at the Institute of Geological Sciences, University of Bern (Switzerland). Rock samples were crushed by using a stainless steel mortar and pestle. They were then dry milled in an agate ring mill for 30 min. Each run of sample was bracketed by sand quartz milling for 15 min in order to clean the receptacle. Nanoparticulate pressed powder pellets (PPPs) were created following the procedure described in Peters and Pettke (2017) by using microcrystalline cellulose as a binder. The PPPs were analysed using a laser ablation inductively coupled plasma mass spectrometer (LA-ICP-MS) consisting of a GeoLas-Pro 193 nm ArF Excimer laser system (Lambda Physik) in combination with an ELAN DRC-e quadrupole mass spectrometer (Perkin Elmer). Calibration was based on GSD-1G (Jochum et al., 2011) reference material. BRP-1 (Cotta et al., 2007) was used as a secondary standard (Peters & Pettke, 2017) and accuracy was always better than 10%. PPPs were measured in single spot mode with an energy density of 6 J/cm<sup>2</sup> at a repetition rate of 10 Hz and a beam size of 90 µm. Six analyses were measured for each PPP. The surface area was cleaned by pre-ablation using a larger spot size and for each analysis the signal was integrated over a 50–60 s. Data reduction was performed offline by using the software SILLS (Guillong et al., 2008) and limits of detection were calculated after Pettke et al. (2012). Internal standardization was done by assuming (a) a fixed total of 100 wt% for major and trace elements, minus volatiles determined by loss on ignition; (b) all Fe is present as Fe<sub>2</sub>O<sub>3</sub>.

## 4.3 | Trace element analysis

LA-ICP-MS mineral analyses were conducted using two different instruments at the Institute of Geological Sciences,

University of Bern (Switzerland). Part of the punctual analyses was achieved with a GeoLas-Pro 193 nm ArF Excimer laser system (Lambda Physik) in combination with an ELAN DRC-e quadrupole mass spectrometer (Perkin Elmer). Mapping and the second part of mineral punctual analyses were conducted using a Resonetics RESolutionSE 193nm excimer laser system equipped with a S-155 large volume constant geometry chamber (Laurin Technic). The laser system was coupled to an Agilent 7900 quadrupole ICP-MS instrument. Calibration was performed using reference material GSD-1G (Jochum et al., 2005), whereas NIST 612 (Jochum et al., 2011) was used as secondary standard with three ablation spots each. Data were reduced offline employing SILLS (Guillong et al., 2008) and Iolite v7.08 (Paton et al., 2011). Drift was linearly corrected by bracketing the unknowns with the calibration material and LODs were calculated according to Pettke et al. (2012). Beam diameter was adapted according to grain size.

On the Resonetics RESolutionSE 193nm excimer laser system garnet was ablated at 5 Hz and a fluence of 4 J/cm<sup>2</sup>, during post-acquisition quantification processing <sup>27</sup>Al was used as internal standard (11 wt%). On the GeoLas-Pro 193 nm ArF Excimer laser system garnet was ablated at 10 Hz and 9 J/cm<sup>2</sup>, during post-acquisition quantification processing internal standardization was done by summing the measured mass fraction of element oxides to 100 wt% assuming garnet as anhydrous phase. Accuracy on secondary standard was better than 10% for all elements.

Rutile was ablated on the GeoLas-Pro 193nm ArF Excimer laser system at 8 Hz and a fluence of 6 J/cm<sup>2</sup>. During post-acquisition quantification processing <sup>49</sup>Ti was used as internal standard (59.94 wt%). Accuracy on secondary standard NIST 612 was within 10% for all elements and 20% for Zr.

Garnet trace element maps were acquired on standard 30 µm thick polished thin sections using a comparable protocol to that described in Raimondo et al. (2017) and George et al. (2018). The laser was operated at a repetition rate of 10 Hz, a fluence of 7 J/cm<sup>2</sup> and a continuous scan speed of 10 µm/s, using a beam diameter of 12 or 16 µm. Line spacing was adapted accordingly to the beam diameter. A total of

31 elements were measured for a total sweep time of 0.46 s, where dwell times were 0.01 s for most masses with the exception of light REE (LREE; from La to Gd = 0.02 s), and Hf (0.03 s). During post-acquisition quantification processing  $^{27}\text{Al}$  was used as internal standard (11 wt%). Image processing was performed using XMapTools 3.2.1.

#### 4.4 | Lu–Hf geochronology

For Lu–Hf garnet geochronology, bulk rock powders and mineral separates were prepared at the Institute of Geological Sciences, University of Bern (Switzerland). High quality mineral separates were obtained by applying high voltage discharge on rock samples using SelFrag Lab system. Mesh size allowing specific mineral fraction separation was adapted for each sample. The fragmented material was then dried in an oven at 60°C. Multi-grain garnet separates were carefully prepared under a binocular microscope. Whole-rock powders were made by crushing rock samples in a stainless steel mortar and pestle. Samples were then dry milled in an agate ring mill for 30 min. Each sample run was bracketed by sandquartz milling for 15 min in order to clean the receptacle. Chemical digestion and isotopic analyses were conducted at the Pacific Centre for Isotope and Geochemical Research, University of British Columbia. Garnet separates and whole-rock powders were weighed in screw-top PFA beakers following admixing of a  $^{176}\text{Lu}$ – $^{180}\text{Hf}$  isotope tracer. Garnet dissolution was done by cycling HF–HNO<sub>3</sub>–HClO<sub>4</sub> and HCl with intermittent solution dry-down. This method dissolves garnet without co-dissolving zircon (Lagos et al., 2007; Scherer et al., 2000). Whole-rock powders were dissolved in HF–HNO<sub>3</sub> kept at 180°C for 5 days in Parr® high-*P* digestion vessels. Solutions containing dissolved mineral and whole-rock chemical matrices were loaded onto pre-conditioned 12 ml Teflon® columns containing Eichrom® Ln-spec resin and Lu and Hf were isolated and purified using the methods of Münker et al. (2001). The Lu and Hf isotope measurements were carried out using a Nu Instruments *Plasma I* multi-collector ICPMS. The  $^{176}\text{Lu}/^{175}\text{Lu}$  of unknowns was determined using  $^{176}\text{Yb}$  interference corrections on the basis of a linear correlation between  $\ln(^{176}\text{Yb}/^{171}\text{Yb})$ – $\ln(^{174}\text{Yb}/^{171}\text{Yb})$ , which was determined by replicate Yb standard measurements (Blichert-Toft et al., 2002). Hafnium mass bias was corrected assuming the exponential law and applying  $^{179}\text{Hf}/^{177}\text{Hf} = 0.7325$ . All Hf isotope ratios are reported relative to JMC-475 ( $^{176}\text{Hf}/^{177}\text{Hf} = 0.282163$ ; Blichert-Toft et al., 1997), for which long-term external reproducibility is 0.3 εHf at the concentration typical of garnet samples. The external reproducibility (2 *SD*) of the  $^{176}\text{Hf}/^{177}\text{Hf}$  of unknowns was estimated on the basis of the external reproducibility for ATI-475—and in-house Hf reference solution that is isotopically identical to, and prepared from the same metal ingots as, JMC-475

( $^{176}\text{Hf}/^{177}\text{Hf} = 0.282160$ ; Blichert-Toft et al., 1997), which was measured at concentrations that bracketed those of the unknowns (Bizzarro et al., 2003). A realistic blanket uncertainty of 0.25% on  $^{176}\text{Lu}/^{177}\text{Hf}$  was assumed. Total procedural Hf blanks during the course of the analytical session were 12 pg or lower. Isochron regressions and age calculations were done using Isoplot version 3.27 (Ludwig, 2003), applying  $1.867 \times 10^{-11} \text{ year}^{-1}$  for  $\lambda^{176}\text{Lu}$  (Scherer et al., 2001; Söderlund et al., 2004). All uncertainties are reported at the 2 *SD* level.

#### 4.5 | Phase equilibrium modelling

The *P*–*T* conditions for garnet formation were determined using the program GrtMod 1.6.2 (Lanari et al., 2017) based on an iterative simulation of garnet growth and resorption. Starting with the bulk rock composition, each stage of garnet growth is modelled for determining *P*–*T* and the amount of fractionated garnet in order to match the observed garnet composition. The modelled garnet composition is obtained by minimizing the Gibbs energy. The input parameters of GrtMod are (a) the bulk rock composition, (b) the amount of water available in the system, (c) the oxidation state of the system, and (d) the number of growth stages each of them having a specific garnet composition. The optimization routine produces for each growth stage ‘optimal’ *P*–*T* conditions and an uncertainty envelope by minimizing the differences between the measured and the modelled garnet compositions while optimizing the reactive bulk composition, which depends on how much garnet is fractionated (i.e. subtracted from the bulk rock composition) or resorbed (i.e. re-injected in the reactive bulk composition). A software option can be used to prevent resorption in case of isolated growth zones, or clear the absence of resorption textures in the sample. Gibbs energy minimizations were performed using Theriak-Domino (De Capitani & Brown, 1987; De Capitani & Petrakakis, 2010) and the internally consistent thermodynamic data set of Holland and Powell (1998) and subsequent updates gathered in tc55 (see below). The chemical system was restricted to SiO<sub>2</sub>–TiO<sub>2</sub>–Al<sub>2</sub>O<sub>3</sub>–FeO–MnO–MgO–CaO–Na<sub>2</sub>O–K<sub>2</sub>O–H<sub>2</sub>O–O<sub>2</sub>. The following solid solution models were used: feldspar (Holland & Powell, 2003); spinel, biotite (White et al., 2007); epidote, cordierite, talc, staurolite, chlorite, carpholite, and garnet (Holland & Powell, 1998); clinopyroxene (Green et al., 2007); chloritoid (White et al., 2000); white mica (Coggon & Holland, 2002); amphibole (Diener et al., 2007). Water saturation was applied to all models and this assumption is also justified for the retrograde stages as the breakdown of lawsonite before garnet growth liberates a significant amount of water. Excess oxygen of 0.005 mol was used for sample Z16TB32 to reproduce the observed mode of epidote. These values were adjusted based on *T*–*X* diagrams.

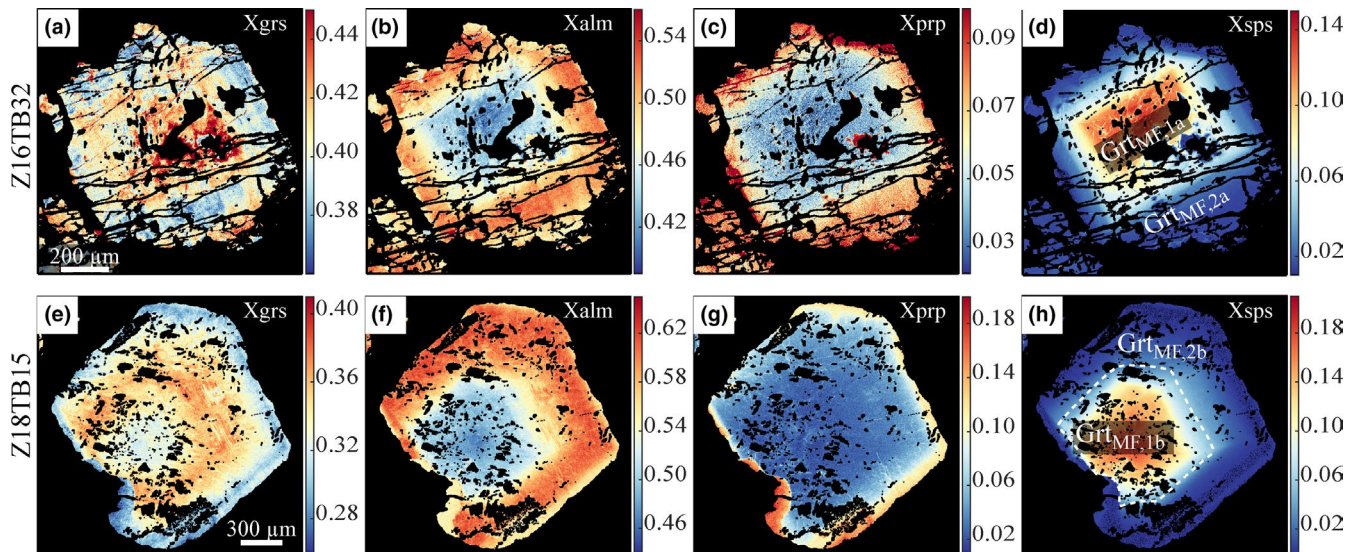


**FIGURE 3** End-member compositional maps of garnet generated using XMapTools (Lanari et al., 2014, 2019) from the mafic granofels sample Z16TB32 (a–d) and sample Z18TB15 (e, f) [Colour figure can be viewed at [wileyonlinelibrary.com](http://wileyonlinelibrary.com)]

For each simulated stage, GrtMod produces the following outputs: (a) the reactive bulk composition, (b) the ‘optimal’  $P$ – $T$  conditions, (c) the modelled garnet composition and (d) the volume of garnet fractionated and resorbed for the actual stage and each of the previous garnet generations. The robustness of the results produced by GrtMod was systematically evaluated as follow: (a) The volume of previous garnet fractionated was compared to observations on each sample; (b) the quality of the solution (i.e. the difference between observed and modelled garnet composition) was monitored using the tolerance factor (TF) with a maximal threshold of 0.05 (e.g. Lanari et al., 2017); and (c) the coexisting minerals predicted to be stable for the same reactive bulk composition were simulated using Theriak-Domino at  $P$ – $T$  condition of garnet equilibrium. The simulated phase assemblage was compared with mineral inclusions observed in garnet.

Two independent methods were applied for white mica thermobarometry. (a) Isopleth intersection, considering Si in atoms per formula unit (a.p.f.u.) and  $X_{Mg}$  ( $X_{Mg} = Mg/(Mg+Fe)$ ), obtained by forward modelling with the software Theriak-Domino. White mica fractionation was not considered as it has no major effect on the modelled compositions (Airaghi et al., 2017). For each compositional group of average  $X_{Mg}$  and Si a.p.f.u. values,  $P$ – $T$  estimates are presented as an ‘optimal’ solution together with an uncertainty envelope obtained using the method of Lanari et al. (2017) adapted here for K-white mica. (b) Inverse models based on the method and solid-solution model of Dubacq et al. (2010) were calculated and plotted using the program ChlMicaEqui (Lanari, 2012). For a given potassic white mica composition in equilibrium with quartz and water, the equilibrium conditions are represented by a line in  $P$ – $T$  space along which the interlayer water content varies (Dubacq et al., 2010).

The  $P$ – $T$  conditions of chloritoid were determined using  $X_{Mg}$  ( $X_{Mg} = Mg/(Mg+Fe)$ ) isopleths modelled with Theriak-Domino.

#### 4.6 | Zr-in-rutile thermometry

Calculations were performed using the ‘combined model’ of Kohn (2020) assuming growth at the maximum pressure determined for our samples (2.65 GPa; see below), thus providing maximum temperature estimates. The sources of uncertainty to be propagated onto Zr-in-rutile temperature estimates are the effect of analytical uncertainty of Zr measurement and uncertainty inherent in the calibration ( $\sim 2\%$  for 500–650°C, Kohn 2020). The Zr analytical error was estimated to be  $\pm 20\%$ , which corresponds to an uncertainty of  $\pm 15$ – $20^\circ\text{C}$  for the 500–650°C temperature range. Combined with the internal error of the calibration of Kohn (2020), a total uncertainty of  $\pm 35^\circ\text{C}$  is estimated for the same temperature range. The presence of quartz and zircon in the schists ensures an activity of  $\text{SiO}_2$  and  $\text{ZrO}_2$  of unity for a robust application of this thermometer.

## 5 | RESULTS

### 5.1 | Mineral texture and chemistry

#### 5.1.1 | Garnet chemistry

Major and trace element compositional maps of garnet from the mafic granofels, mafic schist, and Cld-schist are shown in Figures 3–6 and in Figures S1–S4. Pixels were selected

in specified regions-of-interest to reflect the main chemical zones observed in garnet chemical maps (Figures 3d,h, 4c,g, and 5c). The average composition of each growth zone is reported in Tables S1 and S2.

#### Mafic granulites samples Z16TB32 and Z18TB15

Garnet composition ranges between Grs<sub>30</sub> and Grs<sub>50</sub> with pyrope content below Prp<sub>20</sub>. Garnet cores are systematically enriched in Mn up to Sps<sub>20</sub> in sample Z18TB15 and Sps<sub>15</sub> in Z16TB32. In sample Z16TB32, Ca and Mn decrease from core (Grt<sub>MF,1a</sub>) to rim (Grt<sub>MF,2a</sub>) following a bell-shaped profile that is mirrored by Fe and Mg (Figure 3a–d). Irregular Ca enrichment is observed along rims (Figure 3a). In sample Z18TB15, Mn decreases from core (Grt<sub>MF,1b</sub>) to rim (Grt<sub>MF,2b</sub>) following a bell-shaped profile associated with Fe increase (Figure 3b,h). The distribution of Ca is more complex, with a Ca-poor core, a Ca-rich mantle, and a Ca-poor rim (Figure 3e). The numerous garnet grains investigated locally show a discontinuous 0.2–0.3 mm rim that is enriched in Mg and depleted in Mn, Fe, and Ca (Figure 3e–h). In sample Z18TB15, garnet shows strong concentric trace element zoning, with maximum heavy REE (HREE) concentrations in cores decreasing towards the rim and local patchy Y+HREE enrichment in mantle (Figure 6a and Figure S1). The discontinuous rim defined by major elements (Figure 3e–h) is

enriched in Co, Zn, Y, Eu, middle REE (MREE), and depleted in Ti, V, Cr, and HREE.

#### Mafic schist samples Z16TB11 and Z16TB28

The small garnet grains in the matrix exhibit two chemically distinct zones with a sharp and irregular boundary that is less than 1 μm wide (Figures 4a–d and 7a). The cores (Grt<sub>MS,1</sub>) are enriched in Fe, Mg, and Mn, and depleted in Ca (Alm<sub>64–68</sub>Prp<sub>23–27</sub>Grs<sub>13–15</sub>Sps<sub>1–3</sub>) compared to the rims. Mn enrichment domains are observed along the core–rim boundary (Figure 4d). The euhedral rims are zoned, with an inner part (Grt<sub>MS,2</sub>) that is distinctly richer in Ca and poorer in Mg (Alm<sub>54–59</sub>Prp<sub>5–8</sub>Grs<sub>32–36</sub>Sps<sub>1–2</sub>) than the outer part (Grt<sub>MS,3</sub>, Alm<sub>54–59</sub>Prp<sub>19–22</sub>Grs<sub>21–25</sub>Sps<sub>1–2</sub>). Larger garnet porphyroblasts (Figures 4e–l and 7b) are characterized by smooth concentric zoning, with Mg concentrations increasing and Fe and Mn decreasing towards the rim. Ca zoning is locally more patchy and inhomogeneous in sample Z16TB11. The chemical composition of these porphyroblasts (Alm<sub>54–62</sub>Prp<sub>8–22</sub>Grs<sub>24–32</sub>Sps<sub>1–9</sub>) is similar to that of the rim of matrix garnet, except that Mn core concentrations are slightly higher. In sample Z16TB11, garnet porphyroblasts display only minor trace element zoning (Figure 6b and Figure S2). Euhedral, oscillatory zoning at the 50 μm scale is visible in Cr, Y, and HREE, and sector zoning is

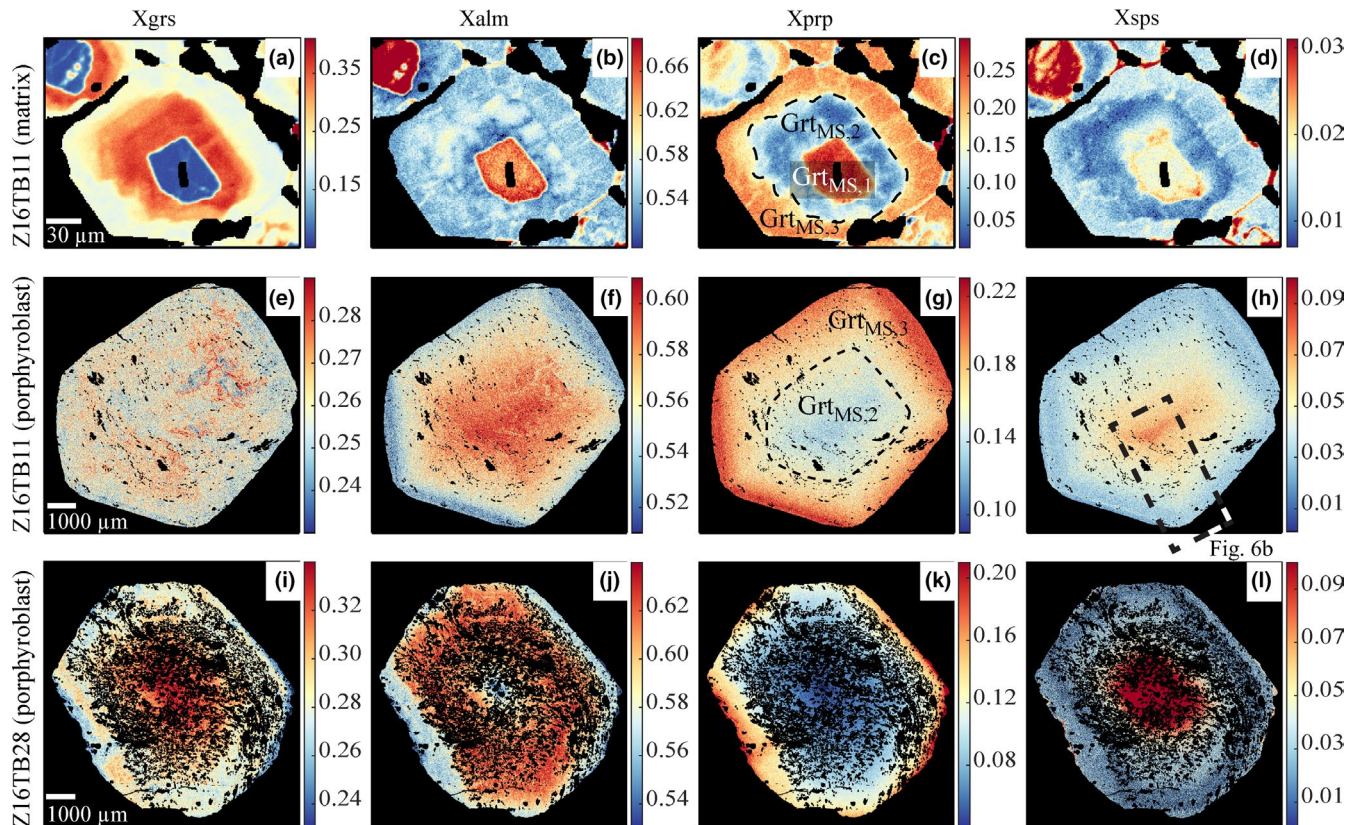


**FIGURE 4** End-member compositional maps of small garnet crystals from the mafic schist sample Z16TB11 (a–d), and garnet porphyroblasts from sample Z16TB11 (e–h) and sample Z16TB28 (i–l) [Colour figure can be viewed at [wileyonlinelibrary.com](http://wileyonlinelibrary.com)]

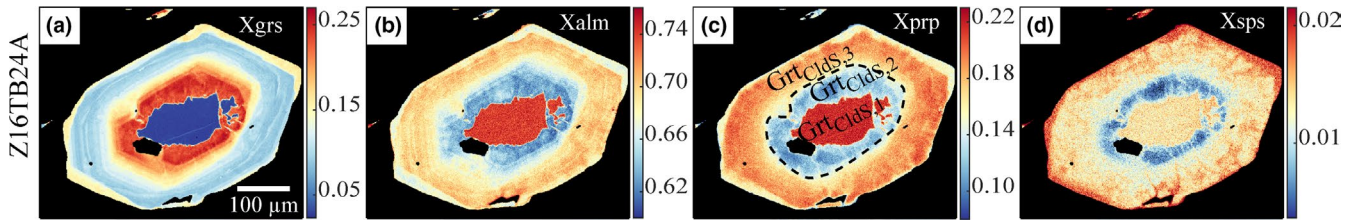


**FIGURE 5** End-member compositional maps of garnets from the Clid-schist sample Z16TB24A [Colour figure can be viewed at [wileyonlinelibrary.com](http://wileyonlinelibrary.com)]

observed for Y and REE within garnet mantle and rim. REE patterns (Figure 8a) show an increase from LREE to MREE, and a flat HREE pattern. The REE pattern of garnet porphyroblasts from sample Z16TB28 (Figure 8c) shows an increase from MREE to HREE and a marked decrease in  $Gd_N/Yb_N$  ( $N = \text{chondrite normalized}$ ) from core to rim. For the small garnet grains that display sharp chemical zoning in major elements the spatial resolution of the ablation spot is insufficient to resolve all the domains. REE normalized patterns (Figure 8b) show comparable HREE composition between core and rim, with a  $Gd_N/Yb_N$  relatively close to unity. The cores are generally richer in MREE and have a marked negative Eu anomaly ( $Eu/Eu^* = Eu_N / (Sm_N * Gd_N)^{0.5}$ ) of  $\sim 0.1$ , which is not observed for the rims.

#### Chloritoid schist sample Z16TB24A

Garnet has two distinct chemical zones (Figures 5 and 7a) separated by a sharp  $1 \mu\text{m}$  contact. The xenomorphic cores ( $Grt_{\text{Cls},1}$ ) are depleted in Ca and enriched in Fe and Mg ( $Alm_{72-76}Prp_{20-24}Grs_{3-6}Sps_1$ ) compared to the rims. The euhedral rims are zoned with decreasing Ca and increasing Mg, Fe, and Mn from the inner ( $Grt_{\text{Cls},2}$ ) to the outer part ( $Grt_{\text{Cls},3}$ ,  $Alm_{54-58}Prp_{15-17}Grs_{26-30}Sps_{0.1-0.2}$  to  $Alm_{60-68}Prp_{8-12}Grs_{23-27}Sps_{<1}$  respectively). A Ca- and Mn-rich discontinuous domain of up to  $15 \mu\text{m}$  width is observed along the external rim. Trace element mapping (Figure 6c and Figure S3) highlights the strong chemical difference between core and rim, as described for major elements. The core is enriched in V, Cr, Li, Co, Y, and HREE compared to the inner rim. The external rim is depleted in V and Ti, and enriched in Cr, Co, and MREE, compared to the inner rim. On a logarithmic scale, the REE patterns of garnet cores and rims largely overlap (Figure 8d) but the core is characterized by lower  $Gd_N$  and a marked Eu negative anomaly of  $\sim 0.2$ , which is not present in the rim.

#### 5.1.2 | K-white mica and chloritoid major element chemistry

The compositional variability of potassic white mica from mafic schists (Z16TB11 and Z16TB28) and the chloritoid schist (Z16TB24A) was investigated. In every sample,

mica flakes are preferentially oriented along the main foliation and microstructural criteria are not sufficient to discriminate different populations. However, the compositional maps reveal variations in the Si a.p.f.u. and  $X_{Mg}$  (Figure 9). Pixels selected in specified regions-of-interest on the Si a.p.f.u. and  $X_{Mg}$  binary plots were adjusted to reflect the main textural domains and allow for a discrimination of several populations of K-white mica in each sample (Figure 9). Representative average K-white mica compositions were extracted from the elemental maps and are reported in Table S3.

#### Mafic schist samples Z16TB11 and Z16TB28

Three K-white mica populations were identified in sample Z16TB11 (Figure 9a,c) and five in Z16TB28 (Figure 9d,f). The three mica populations of Z16TB11 ( $Ph_{MS,1a}$ ,  $Ph_{MS,2a}$ , and  $Ph_{MS,3a}$ ) are phengite and have comparable microtextural location and spatial distribution than the three-first population of Z16TB28 ( $Ph_{MS,1b}$ ,  $Ph_{MS,2b}$ , and  $Ph_{MS,3b}$ ). The first mica population ( $Ph_{MS,1a}$  and  $Ph_{MS,1b}$ ) is located in the central zone of elongated mica flakes stretched along the main foliation. It has on average  $3.33 \pm 0.02$  Si a.p.f.u. and  $0.76 \pm 0.02$   $X_{Mg}$  in sample Z16TB11 and  $3.40 \pm 0.02$  Si a.p.f.u. and  $0.79 \pm 0.02$   $X_{Mg}$  in sample Z16TB28. The second population of mica ( $Ph_{MS,2a}$  and  $Ph_{MS,2b}$ ) occurs either on the edge of the first population clusters or as single grains in the foliation. It has on average Si a.p.f.u. of  $3.29 \pm 0.02$  and  $X_{Mg}$  of  $0.71 \pm 0.02$  in sample Z16TB11 and Si a.p.f.u. of  $3.34 \pm 0.02$  and  $X_{Mg}$  of  $0.72 \pm 0.02$  in sample Z16TB28. The third mica group ( $Ph_{MS,3a}$  and  $Ph_{MS,3b}$ ) is found on the edge of the second population clusters or as isolated grains. The Si a.p.f.u. content is  $3.22 \pm 0.02$  and  $X_{Mg}$  is  $0.66 \pm 0.02$  in sample Z16TB11 and Si a.p.f.u. of  $3.24 \pm 0.02$  and  $X_{Mg}$  of  $0.64 \pm 0.02$  in sample Z16TB28. The last two populations of K-white mica ( $Kwm_{MS,1}$  and  $Kwm_{MS,2}$ ) are only observed in Z16TB28 and are characterized by a lower Si a.p.f.u. than the three previous generations (Figure 9d). They are texturally associated with zoisite and paragonite, and form patchy aggregates, which sometimes rim the previously described mica population (Figure 9f). On average,  $Kwm_{MS,1}$  Si a.p.f.u. content is  $3.11 \pm 0.02$  and  $X_{Mg}$  is  $0.78 \pm 0.02$ , whereas  $Kwm_{MS,2}$  Si a.p.f.u. content is  $3.12 \pm 0.02$  and  $X_{Mg}$  is  $0.67 \pm 0.02$ .

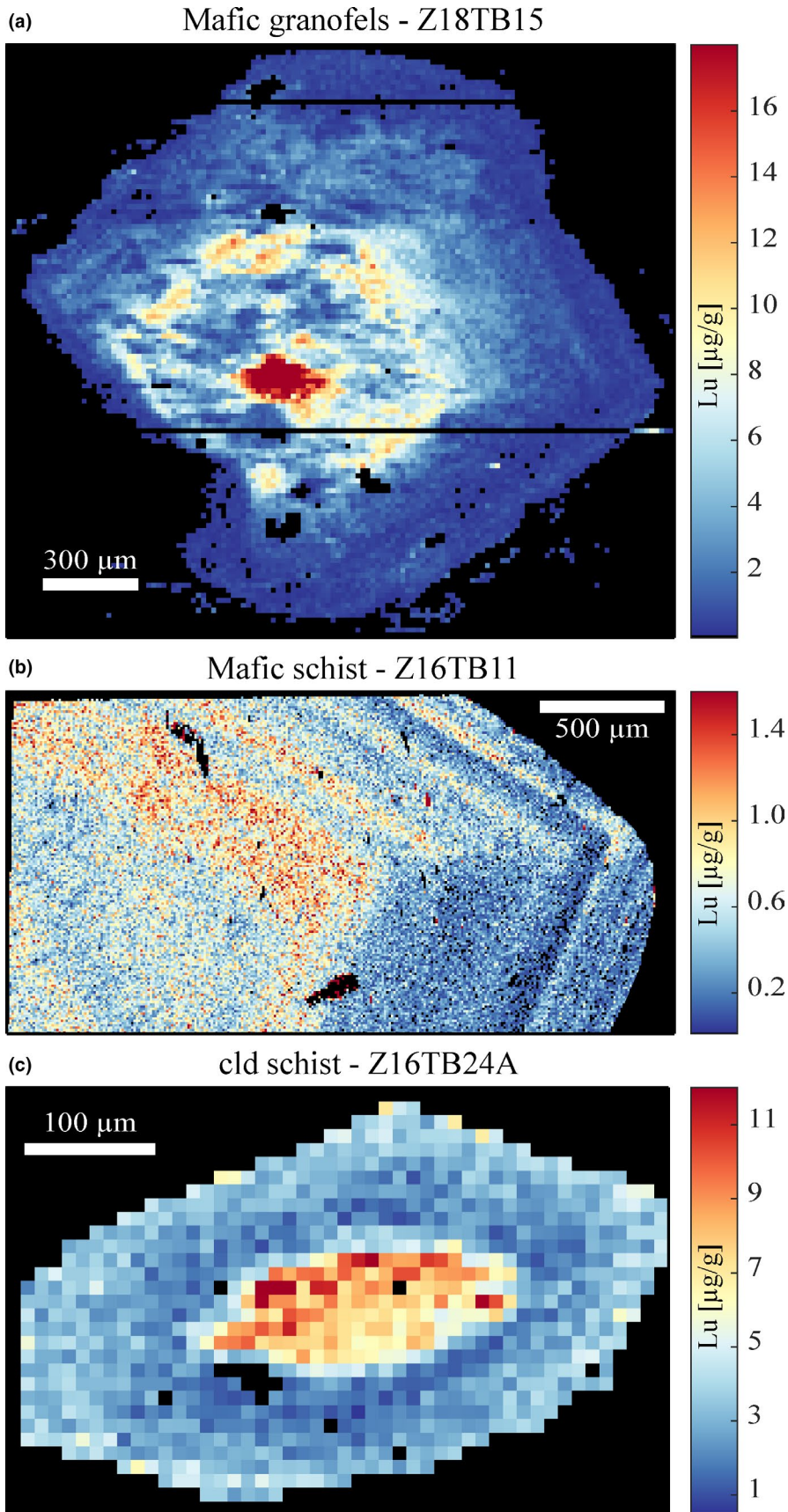


**FIGURE 6** Trace element LA-ICP-MS compositional maps of Lu in garnet for the three rock types dated by Lu–Hf. For the mafic schist, Lu distribution in Z16TB11 is interpreted as representative for the dated sample Z16TB28 (see text) [Colour figure can be viewed at [wileyonlinelibrary.com](http://wileyonlinelibrary.com)]

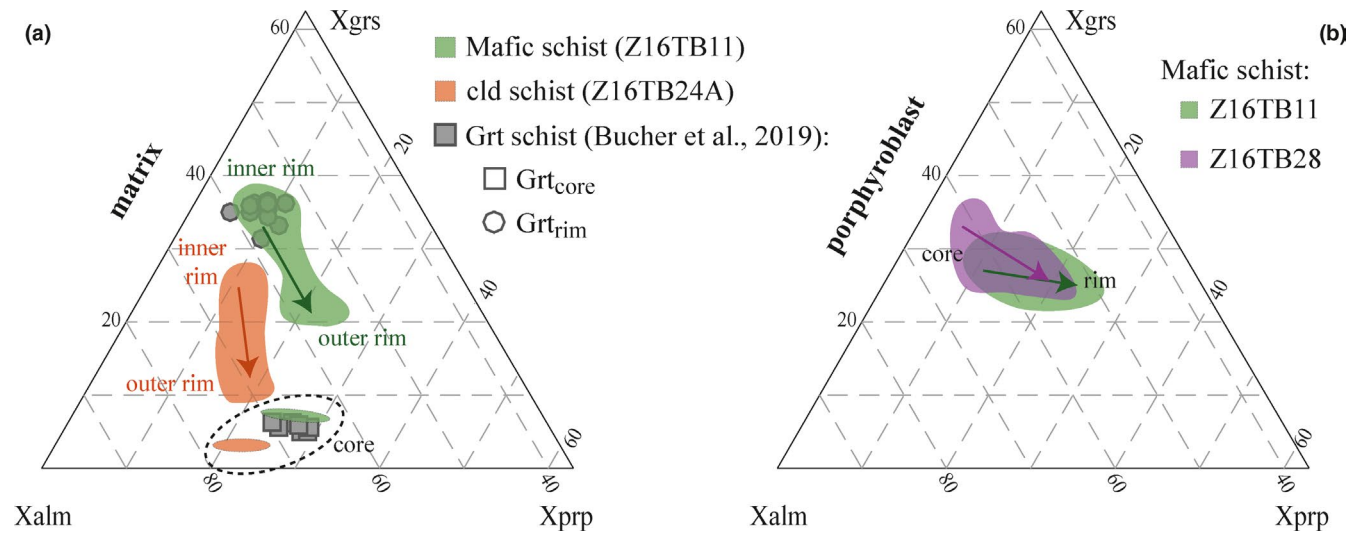


**FIGURE 7** Ternary chemical diagram showing the range of garnet composition in  $X_{\text{grs}}-X_{\text{alm}}-X_{\text{prp}}$ . Range of compositional data was exported from compositional maps (Figure S6). (a) Small garnet grains from the mafic schist (Z16TB11, area drawn on the basis of 30137 pixels) and Cld-schist (Z16TB24A, area drawn on the basis of 111072 pixels), compared with garnet compositions from Bucher et al. (2019). (b) Garnet porphyroblasts from the mafic schist samples Z16TB11 (area drawn on the basis of 516869 pixels) and Z16TB28 (area drawn on the basis of 209512 pixels) [Colour figure can be viewed at [wileyonlinelibrary.com](http://wileyonlinelibrary.com)]

#### Chloritoid schist sample Z16TB24A

Two populations of K-white mica were identified (Figure 9g). The first population of phengite ( $\text{Ph}_{\text{CldS},1}$ ) is located in the central zone of elongated mica aggregates stretched along the main foliation (Figure 9i). It has on average  $3.38 \pm 0.02$  Si a.p.f.u. and  $0.72 \pm 0.02$   $X_{\text{Mg}}$ . The second population of phengite ( $\text{Ph}_{\text{CldS},2}$ ) occurs either on the edge of the first population clusters or as single grains in the foliation. It has on average Si a.p.f.u. of  $3.28 \pm 0.02$  and  $X_{\text{Mg}}$  of  $0.65 \pm 0.02$ . Chloritoid from the Cld-schist (Table S4) varies in  $X_{\text{Mg}}$  from 0.25 to 0.38, where higher values are representative of the core and decrease towards the external part of the rim (Figure S5).

#### 5.1.3 | Rutile

Among the studied samples, rutile was found in the mafic and Cld-schist with a grain size varying from a few to 100  $\mu\text{m}$ . All analysed rutile grains were located in the matrix except two grains found as inclusions in garnet (mafic schist Z16TB11 and Z16TB28). Grains for analyses were carefully selected to avoid possible contamination by inclusions and fractures. Analyses (Table S5) were screened for contamination from inclusions based on high Si, Na, Al, Mn, Fe, Y, Sn, Hf, and Zr contents. The average concentration of Zr in rutile (Table 2) within the mafic schist is  $36 \pm 3$   $\mu\text{g/g}$  in sample Z16TB11 and  $40 \pm 4$   $\mu\text{g/g}$  in sample Z16TB28. Rutile inclusions in garnet contain 36  $\mu\text{g/g}$  (sample Z16TB11) and 27  $\mu\text{g/g}$  (sample Z16TB28) Zr. The average Zr concentration in the rutile from Cld-schist (sample Z16TB24A) is  $40 \pm 5$   $\mu\text{g/g}$ . The Zr

concentration in rutile is similar within uncertainty among the different lithologies.

## 5.2 | Thermobarometry

### 5.2.1 | Thermodynamic modelling

The  $P$ - $T$  stability conditions of garnet, phengite, and chloritoid were determined for the investigated samples using the strategy outlined in Section 4.5; results are shown in Figures 9–11 and Table 3. The reactive bulk compositions used are reported in Table S6. After careful identification of representative chemical garnet zones in each sample, average garnet chemical compositions were extracted from the elemental maps (Table S1) from the domains shown in Figures 3d,h, 4c,g, and 5c. Minor chemical variations within the domains for sample Z18TB15, Z16TB24A, and Z16TB11 were not considered.

#### Mafic granofels sample (Z16TB32)

The garnet core  $\text{Grt}_{\text{MF},1a}$  (Figure 3d) is predicted to be stable at  $490 \pm 10^\circ\text{C}$  and  $1.74 \pm 0.05$  GPa (TF: 0.011) with 5 vol.% of garnet (Figure 10a). The modelled phase assemblage is  $\text{Grt}+\text{Omp}+\text{Chl}+\text{Bt}+\text{Tr}+\text{Lws}+\text{Ttn}+\text{Qz}$ . The rim stage  $\text{Grt}_{\text{MF},2a}$  (Figure 3d) is modelled at  $570 \pm 10^\circ\text{C}$  and  $2.52 \pm 0.10$  GPa (TF: 0.023; 8 vol.% garnet) while preventing resorption of  $\text{Grt}_{\text{MF},1a}$  (Figure 10a). The modelled phase assemblage at these conditions is  $\text{Grt}+\text{Omp}+\text{Ph}+\text{Lws}+\text{Qz}+\text{Rt}$ .

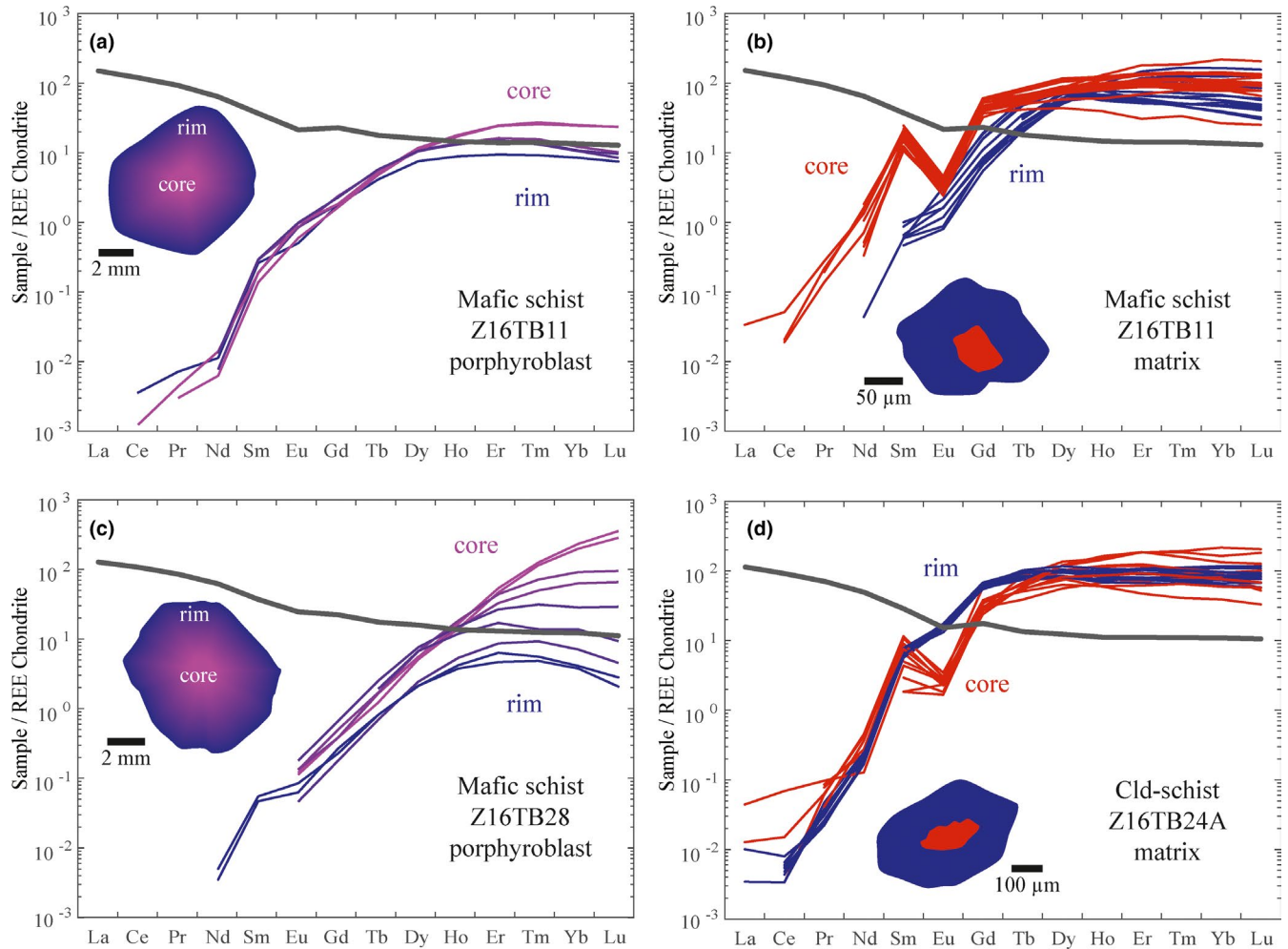


**FIGURE 8** REE chondrite-normalized concentrations of bulk rock (black) and garnet (red, violet, and blue) from different samples. Normalization data: Taylor and McLennan (1985) [Colour figure can be viewed at [wileyonlinelibrary.com](http://wileyonlinelibrary.com)]

#### *Mafic granofels sample (Z18TB15)*

The garnet core  $\text{Grt}_{\text{MF},1\text{b}}$  (Figure 3h) is predicted to be stable at  $486 \pm 15^\circ\text{C}$  and  $1.81 \pm 0.05$  GPa (TF: 0.046) with 2 vol.% of garnet (Figure 10b). The modelled phase assemblage is  $\text{Grt}+\text{Omp}+\text{Chl}+\text{Bt}+\text{Tr}+\text{Lws}+\text{Qz}+\text{Rt}$ . The rim stage  $\text{Grt}_{\text{MF},2\text{b}}$  (Figure 3h) is modelled at  $590 \pm 15^\circ\text{C}$  and  $1.65 \pm 0.15$  GPa (TF: 0.003) with the formation of 21 vol.% of garnet without requiring resorption of  $\text{Grt}_{\text{MF},1\text{b}}$  (Figure 10b). The modelled phase assemblage at these conditions is  $\text{Grt}+\text{Omp}+\text{Ms}+\text{Tr}+\text{Zo}+\text{Qz}+\text{Rt}$ .

#### *Mafic schists (sample Z16TB11)*

The garnet core composition  $\text{Grt}_{\text{MS},1}$  (Figure 5c) is modelled at a temperature of  $591 \pm 10^\circ\text{C}$  and pressure ranging between 2.65 and 2.85 GPa with optimal solution at 2.65 GPa (TF: 0.039). The modelled phase assemblage is  $\text{Grt}+\text{Omp}+\text{Ph}+\text{Gln}+\text{Ky}+\text{Lws}+\text{Qz}+\text{Rt}$  (Figure S7) and contains 19 vol.% of garnet (Figure 10c). Simulation for the inner rim stage  $\text{Grt}_{\text{MS},2}$  (Figure 5c) predicts strong resorption of  $\text{Grt}_{\text{MS},1}$  (17 vol.%) and leads to the formation of 6 vol.% of garnet  $\text{Grt}_{\text{MS},2}$  (Figure 10c) at  $553 \pm 10/-50^\circ\text{C}$  and

$1.47 \pm 0.15/-0.35$  GPa (TF: 0.059). The modelled phase assemblage for  $\text{Grt}_{\text{MS},2}$  is  $\text{Grt}+\text{Chl}+\text{Pg}+\text{Bt}+\text{Gln}+\text{Zo}+\text{Qz}+\text{Rt}$  (Figure S8). The simulation for the external rim  $\text{Grt}_{\text{MS},3}$  (Figure 5c) predicts the observed garnet composition at  $595 \pm 25/-10^\circ\text{C}$  and  $1.80 \pm 0.05/-0.30$  GPa (TF: 0.034). Previously fractionated garnet stages are only slightly affected with 1 vol.% resorption of  $\text{Grt}_{\text{MS},1}$ , with up to 14 vol.% garnet fractionation of  $\text{Grt}_{\text{MS},3}$  (Figure 10c). The modelled phase assemblage is  $\text{Grt}+\text{Chl}+\text{Ph}+\text{Pg}+\text{Gln}+\text{Zo}+\text{Qz}+\text{Rt}$  (Figure S9). Intersection of Si a.p.f.u. and  $X_{\text{Mg}}$  isopleths in phengite (Figure 9b) is observed at  $590 \pm 15^\circ\text{C}$  and  $2.5 \pm 0.1$  GPa for  $\text{Ph}_{\text{MS},1\text{a}}$ . The second population  $\text{Ph}_{\text{MS},2\text{a}}$  is modelled at lower pressure and slightly lower temperature of  $2.0 \pm 0.1$  GPa and  $550 \pm 10^\circ\text{C}$  respectively. The last group  $\text{Ph}_{\text{MS},3\text{a}}$  shows lower pressure conditions ( $1.6 \pm 0.1$  GPa) and similar temperature ( $560 \pm 10^\circ\text{C}$ ) compared to  $\text{Ph}_{\text{MS},2\text{a}}$ . Assuming similar temperature for each population phengite–quartz–water method provides pressure estimates of  $2.2 \pm 0.1$  GPa ( $590 \pm 15^\circ\text{C}$ ,  $\text{Ph}_{\text{MS},1\text{a}}$ ),  $1.8 \pm 0.1$  GPa ( $550 \pm 10^\circ\text{C}$ ,  $\text{Ph}_{\text{MS},2\text{a}}$ ), and  $0.5 \pm 0.1$  GPa ( $560 \pm 10^\circ\text{C}$ ,  $\text{Ph}_{\text{MS},3\text{a}}$ ).

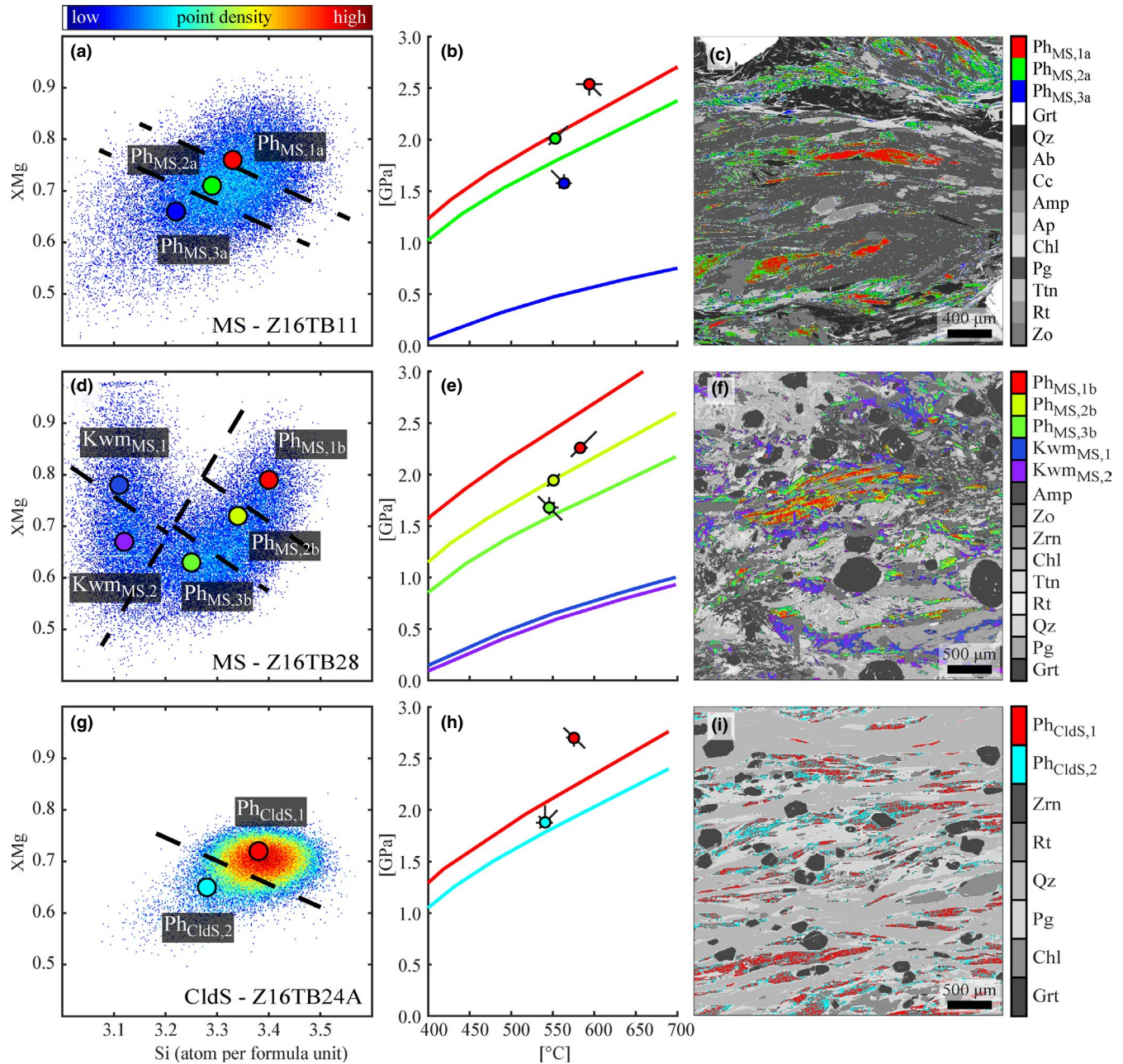


**FIGURE 9** K-white mica population discrimination plots. Each row corresponds to a sample: mafic schist Z16TB11 (a–c), mafic schist Z16TB28 (d–f), Cld-schist Z16TB24A (g–i). First column: Si (atom per formula unit)— $X_{Mg}$  binary diagram with colour scale corresponding to point density (log-scale). Spots show the average composition of each K-white mica group used for modelling. Dashed lines represent the boundary between the different compositional groups. Second column:  $P$ – $T$  estimates based on mica compositions. The spots represent the intersection between  $X_{Mg}$  and Si a.p.f.u. isopleths, whereas lines correspond to phengite–quartz–water equilibria (see text). Third column: spatial relation among K-white mica groups and other phases (in grey) [Colour figure can be viewed at [wileyonlinelibrary.com](http://wileyonlinelibrary.com)]

#### Mafic schist sample Z16TB28

Si a.p.f.u. and  $X_{Mg}$  isopleths of phengite (Figure 9e) intersect at  $580 \pm 20/-15^\circ\text{C}$  and  $2.3 \pm 0.3/-0.1$  GPa for the first group Ph<sub>MS,1b</sub>, and  $550 \pm 10^\circ\text{C}$  and  $2.0 \pm 0.1$  GPa for the second group Ph<sub>MS,2b</sub>. The third population Ph<sub>MS,3b</sub> is modelled at  $550 \pm 10^\circ\text{C}$  and  $1.7 \pm 0.1$  GPa, thus at lower pressure conditions compared to Ph<sub>MS,2b</sub>. Assuming similar temperature for each population, the

phengite–quartz–water method retrieved pressures of  $2.6 \pm 0.1$  GPa ( $580 \pm 20^\circ\text{C}$ , Ph<sub>MS,1b</sub>),  $2.0 \pm 0.1$  GPa ( $550 \pm 10^\circ\text{C}$ , Ph<sub>MS,2b</sub>), and  $1.6 \pm 0.1$  GPa ( $550 \pm 10^\circ\text{C}$ , Ph<sub>MS,3b</sub>). Populations Kw<sub>MS,1</sub> and Kw<sub>MS,2</sub> can only be modelled using the method of Dubacq et al. (2010)—there is no intersection of the isopleths in the  $P$ – $T$  space—and both indicate much lower pressure conditions below 1 GPa (Figure 9e).

TABLE 2 Thermometric estimates determined by Zr-in-rutile thermometry (Kohn, 2020)

Lithology	Sample	N	Zr-rutile ( $\mu\text{g/g}$ )				Pressure (GPa)	Zr-in-Rutile T ( $^{\circ}\text{C}$ )			
			Min	Max	Average	SD		Min	Max	Average	Error
Matrix											
Mafic schist	Z16TB11	16	31	40	36	3	2.65	524	540	534	35
Mafic schist	Z16TB28	25	33	49	40	4	2.65	528	555	541	35
Cld-schist	Z16TB24A	24	31	49	40	5	2.65	524	555	541	35
Inclusion in garnet											
Mafic schist	Z16TB11	1	-	-	36	-	2.65	-	-	534	35
Mafic schist	Z16TB28	1	-	-	27	-	2.65	-	-	515	35

Number of grain analysed (N), minimum (Min), maximum (Max), standard deviation (SD).

### Chloritoid schist sample Z16TB24A

The garnet core composition  $\text{Grt}_{\text{CldS},1}$  (Figure 4c) is predicted to be stable at  $576 \pm 10^{\circ}\text{C}$  and  $2.70 + 0.30/-0.10$  GPa (TF: 0.046). The modelled phase assemblage is  $\text{Grt}+\text{Omp}+\text{Car}+\text{Ph}+\text{Ky}+\text{Lws}+\text{Qz}+\text{Rt}$ , and contains 11 vol.% of garnet (Figure 10d). Simulation of the inner rim stage  $\text{Grt}_{\text{CldS},2}$  (Figure 4c) indicates resorption of previous stage  $\text{Grt}_{\text{CldS},1}$  (7 vol.%) and the formation of 6 vol.% of garnet  $\text{Grt}_{\text{CldS},2}$  (Figure 10d) at  $573^{\circ}\text{C} + 10/-30^{\circ}\text{C}$  and  $1.49 \pm 0.10$  GPa (TF: 0.048). The modelled phase assemblage is  $\text{Grt}+\text{Chl}+\text{Ph}+\text{Pg}+\text{Bt}+\text{Qz}+\text{Rt}$ . The simulation for the external rim  $\text{Grt}_{\text{CldS},3}$  (Figure 4c) is modelled at  $585 \pm 10^{\circ}\text{C}$  and  $2.05 + 0.05/-0.40$  GPa (TF: 0.049). Previously formed garnet growth zones are slightly affected with 2 vol% resorption of  $\text{Grt}_{\text{CldS},1}$  and 3 vol.% of  $\text{Grt}_{\text{CldS},2}$  respectively (Figure 10d). The associated paragenesis is  $\text{Grt}+\text{Ctd}+\text{Ph}+\text{Pg}+\text{Gln}+\text{Qz}+\text{Rt}$ . The intersection of Si a.p.f.u. and  $X_{\text{Mg}}$  phengite isopleths (Figure 9h) provides conditions of  $570 \pm 10^{\circ}\text{C}$  and  $2.7 \pm 0.1$  GPa for  $\text{Ph}_{\text{CldS},1}$  and  $540 \pm 10^{\circ}\text{C}$  and  $1.9 \pm 0.1$  GPa for  $\text{Ph}_{\text{CldS},2}$ . Assuming a similar temperature for each population the phengite–quartz–water method indicates pressure of  $2.3 \pm 0.1$  GPa ( $570 \pm 10^{\circ}\text{C}$ ,  $\text{Ph}_{\text{CldS},1}$ ) and  $1.9 \pm 0.1$  GPa ( $540 \pm 10^{\circ}\text{C}$ ,  $\text{Ph}_{\text{CldS},2}$ ). The  $X_{\text{Mg}}$  isopleth of chloritoid (Figure 11a) is compatible with chloritoid core formation at  $580 \pm 10^{\circ}\text{C}$  between 1.8 and  $2.5 \pm 0.1$  GPa. The external rim is modelled between 1.5 and  $2.5 \pm 0.1$  GPa for a temperature of  $550 \pm 10^{\circ}\text{C}$ .

### 5.3 | Zr-in-rutile thermometry

Zr-in-rutile temperatures were calculated assuming a pressure of 2.65 GPa to provide an independent constraint on the temperature (Table 2). Averaged temperature estimates for rutile found in the mafic schist are  $534 \pm 35^{\circ}\text{C}$  for sample

Z16TB11 and  $541 \pm 35^{\circ}\text{C}$  for sample Z16TB28. The two rutile grains found as inclusions in garnet gave  $534 \pm 35^{\circ}\text{C}$  (sample Z16TB11) and  $515 \pm 35^{\circ}\text{C}$  (sample Z16TB28) respectively. In the Cld-schist (sample Z16TB24A) the average estimated temperature is  $541 \pm 35^{\circ}\text{C}$ . These results witness homogeneous temperature of crystallization among the lithologies of TGU. The dependence of the Zr-in-rutile thermometer on pressure implies that these are maximum temperature for rutile formation.

### 5.4 | Garnet Lu-Hf chronology

The garnet crystals observed in the different lithologies of the TGU present high variability in size, composition, and texture. Key samples were selected (Figure S10) to correlate the garnet size fraction with garnet compositional zoning. In the mafic granofels sample Z18TB15, the compositional zoning in garnet is comparable among all the grains at a sample scale and two garnet fractions were selected, the first one having a diameter between 0.25 and 0.50 mm and the second comprising larger grains ( $>0.50$  mm). Four garnet fractions, comprising two from either size fraction, yielded a Lu–Hf age of  $50.3 \pm 0.3$  Ma (mean square weighted deviation [MSWD] = 1.5; Figure 12a).

Two garnet types were targeted for the schists (Z16TB28 and Z16TB24A). In the mafic schist Z16TB28, garnet porphyroblasts do not show complex textures and have a restricted compositional range. In sample Z16TB28, garnet grains with diameter over 2 mm were picked. The material yielded a Lu–Hf age of  $49.6 \pm 0.8$  Ma (MSWD = 0.34;  $n = 3$ ; Figure 12b). Small garnets with complex and sharp chemical zoning are present in the Cld-schist Z16TB24A and in mafic schist. This garnet type was picked in the Cld-schist because this is the only garnet type observed

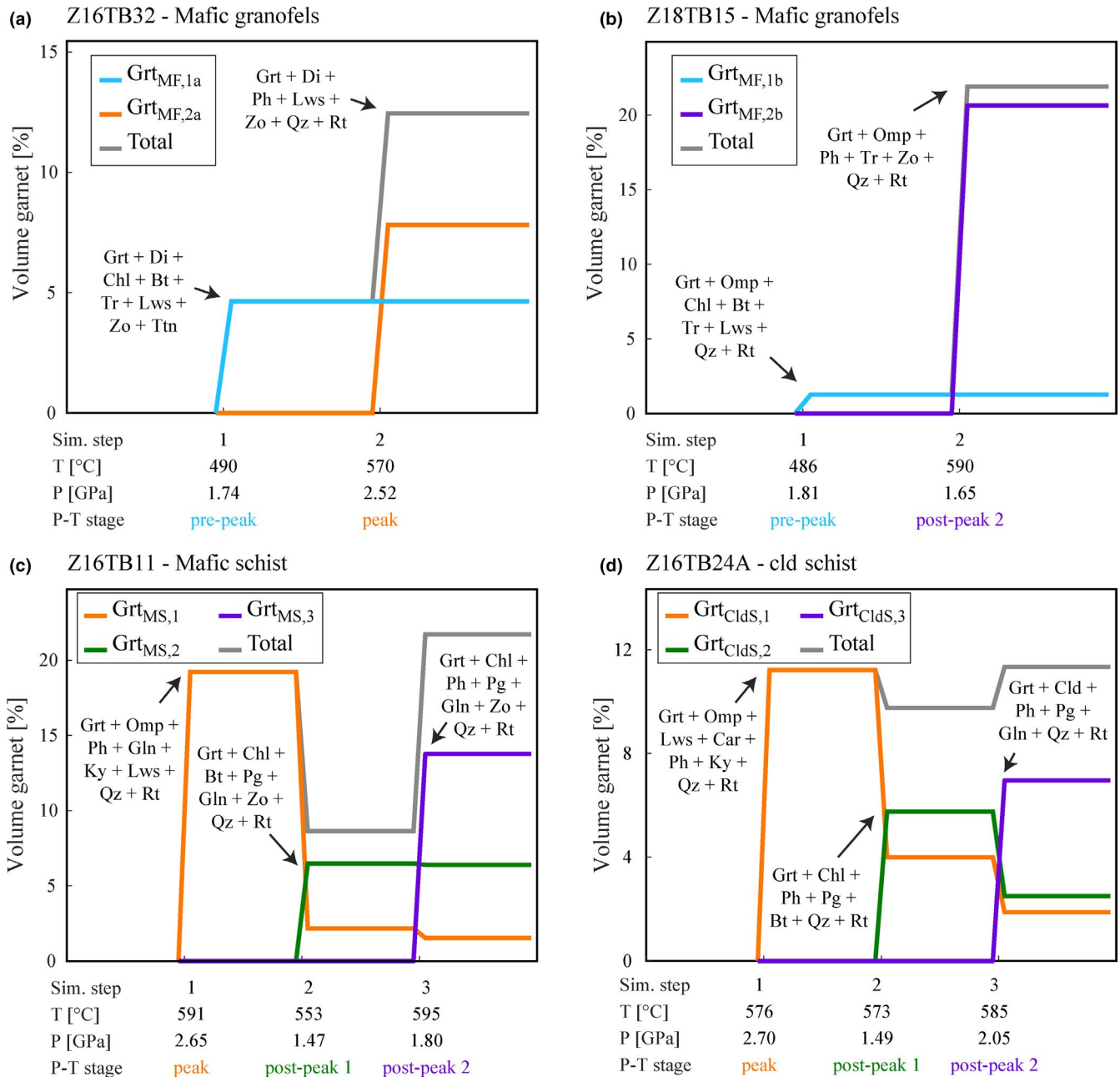


**FIGURE 10** Garnet growth/resorption history for different samples obtained using GrtMod. The evolution of volume fraction (vol.%) of each growth zone are plotted for each step. The curve labelled ‘Total’ shows the evolution of the total amount of garnet in the system. The  $P$ – $T$  conditions of each step are the optimal conditions determined by the model. The modelled mineral assemblages are indicated for each garnet growth step [Colour figure can be viewed at [wileyonlinelibrary.com](https://onlinelibrary.wiley.com)]

in this lithology. Two garnet fractions were differentiated in sample Z16TB24A: the first fraction contains garnet grains with diameter between 250 and 500  $\mu\text{m}$  and the second garnet grains with diameter  $>500 \mu\text{m}$ . The sample yielded a Lu–Hf age of  $48.8 \pm 0.1 \text{ Ma}$  (MSWD = 1.4;  $n = 4$ ; Figure 12c). All samples yielded Lu–Hf dates with uncertainties of 1%RSD or better (Table 4). The relatively high  $^{176}\text{Lu}/^{177}\text{Hf}$  for Z18TB15 ( $>4$ ) and Z16TB24A ( $>13$ ) returned extremely good precision of  $\pm 0.3\%$ RSD and  $\pm 0.2\%$ RSD respectively.

## 6 | DISCUSSION

### 6.1 | Mineral sequence and $P$ – $T$ path of the TGU

The multiple, independent  $P$ – $T$  constraints obtained from the TGU samples can be divided into peak- $P$  metamorphic conditions and conditions that represent earlier (pre-peak) and later (post-peak) metamorphism (Figures 10 and 11a, Table 3). These distinct metamorphic stages were determined

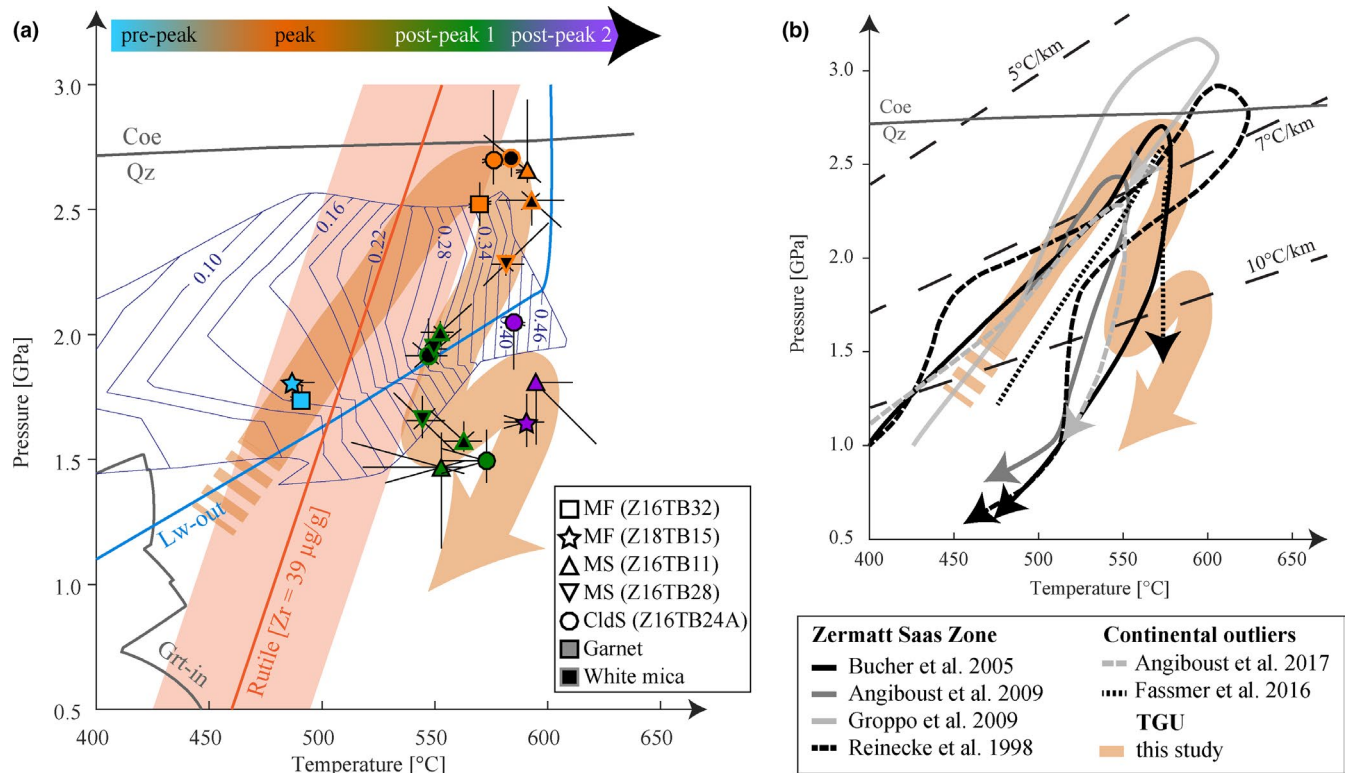


**FIGURE 11** Pressure–temperature path of the TGU and the ZSZ tectonic unit. (a) Synthetic  $P$ - $T$  diagram compiling the thermobarometric results from the four investigated samples. Abbreviation for the lithologies are: MF—mafic granofels, MS—mafic schist, CldS—Cld-schist. Theriak-Domino results: (i) isopleths shown in blue are  $X_{Mg}$  in chloritoid (Cld-schist, Z16TB24A); (ii) The Grt-in curve (mafic granofels, Z18TB15) is shown in grey. (b)  $P$ - $T$  diagram showing a compilation of published  $P$ - $T$  paths from other localities in the ZSZ tectonic unit and published  $P$ - $T$  path from continental outlier in the vicinity of the TGU [Colour figure can be viewed at [wileyonlinelibrary.com](http://wileyonlinelibrary.com)]

according to  $P$ - $T$  estimates simulated in the different mineral growth zones described previously.

Pre-peak metamorphic conditions are inferred from the numerical simulation of garnet for the mafic granofels samples Z16TB32 and Z18TB15. Garnet cores Grt<sub>MF,1a</sub> and Grt<sub>MF,1b</sub> record the earliest growth of garnet at  $P$ - $T$  conditions of  $490 \pm 15^\circ\text{C}$  and  $1.75 \pm 0.05$  GPa (Figure 11a). Equilibrium phase diagram calculations using pristine bulk rock compositions show that the garnet-in curve is at a temperature that is  $\sim 50^\circ\text{C}$  lower than these values (Figure 11a). This discrepancy could be explained either by overstepping to provide the driving force necessary for porphyroblast nucleation and growth (Spear, 2017; Spear & Pattison, 2017; Spear & Wolfe, 2019; Wolfe & Spear, 2018) or off-centre sectioning of garnet. This would have particular impact on the apparent Mn concentration of the garnet nucleus, which is essential to constrain the initiation of the metamorphic growth based on equilibrium thermodynamic modelling (Lanari et al., 2017).

At the mineral scale, fluid–rock interaction commonly leads to fracturing (Angiboust et al., 2011; Giuntoli, Lanari, Burn, et al., 2018; Giuntoli et al., 2018) and pseudomorphic (and commonly non-isochemical) replacement via interface-coupled dissolution and re-precipitation (Konrad-Schmolke et al., 2018; Putnis, 2002), which may overprint previous

chemical information. At the sample scale such fluid–rock interactions could modify the bulk rock composition. These issues are the prime reason why later metasomatism can compromise the reliability of thermodynamic models based on the bulk rock composition (Evans, 2004). In our samples, garnet textures in mafic schists (Figure 4a–d) and Cld-schist (Figure 5), as well as oxygen isotope variations in garnet (Bovay et al., 2021), suggest strong fluid–rock interaction in the post-peak stage. It is thus possible that, of the two garnet generations observed, only the latest stage (Grt<sub>MS,2</sub>, Grt<sub>MS,3</sub>, Grt<sub>CldS,2</sub>, and Grt<sub>CldS,3</sub>) represents an equilibrium with the bulk rock as measured. Nevertheless, the  $P$ - $T$  conditions estimated for peak- $P$  metamorphism ( $580 \pm 15^\circ\text{C}$  and  $2.65 \pm 0.10$  GPa) are in remarkable agreement across lithology. These results are consistent with maximum Zr-in-rutile temperature estimates retrieved from homogeneous rutile populations present in different schist samples (Figure 11a). Moreover, K-white mica found in the mafic schist and in the Cld-schist also record similar peak- $P$  metamorphism conditions (Figure 11a), as determined on the basis of two independent methods: (a) the pressure dependency of Si a.p.f.u. content and the temperature dependency of  $X_{Mg}$  in phengite (Massonne & Schreyer, 1987), and (b) the quartz–water–phengite barometer of Dubacq et al. (2010). Potassic white

TABLE 3 Results of the thermodynamic modelling (Garnet and Phengite)

Rock type	Mafic granofels		Mafic schist		Cld-schist		
	Z16TB32	Z18TB15	Z16TB11	Z16TB28	Z16TB24A		
Mineral	garnet	garnet	garnet	phengite	garnet	phengite	
Method	GrtMod	GrtMod	GrtMod	Isopleth	Inverse modelling	Isopleth	Inverse modelling
Pre-peak							
Population	Grt <sub>MF,1a</sub>	Grt <sub>MF,1b</sub>					
<i>T</i> (°C)	490 ± 10	486 ± 15					
<i>P</i> (GPa)	1.74 ± 0.05	1.81 ± 0.05					
Peak							
Population	Grt <sub>MF,2a</sub>		Grt <sub>MS,1</sub>	Ph <sub>MS,1a</sub>	Ph <sub>MS,1b</sub>	Grt <sub>CldS,1</sub>	Ph <sub>CldS,1</sub>
<i>T</i> (°C)	570 ± 10		591 ± 10	590 ± 15	580 + 20/−15	576 ± 10	570 ± 10
<i>P</i> (GPa)	2.52 ± 0.10		2.65 + 0.20/−0.05	2.5 ± 0.1	2.3 + 0.3/−0.1	2.70 + 0.30/−0.10	2.7 ± 0.1
Post-peak 1							
Population			Grt <sub>MS,2</sub>	Ph <sub>MS,2a</sub>	Ph <sub>MS,2b</sub>	Grt <sub>CldS,2</sub>	Ph <sub>CldS,2</sub>
<i>T</i> (°C)			553 + 10/−50	550 ± 10	550 ± 10	573 + 10/−30	540 ± 10
<i>P</i> (GPa)			1.47 + 0.15/−0.35	2.0 ± 0.1	2.0 ± 0.1	1.49 ± 0.10	1.9 ± 0.1
Population				Ph <sub>MS,3a</sub>	Ph <sub>MS,3b</sub>	Ph <sub>MS,3b</sub>	Ph <sub>CldS,2</sub>
<i>T</i> (°C)				560 ± 10	550 ± 10	(550 ± 10)*	(540 ± 10)*
<i>P</i> (GPa)				1.6 ± 0.1	1.7 ± 0.1	0.5 ± 0.1	1.9 ± 0.1
Post-peak 2							
Population		Grt <sub>MF,2b</sub>	Grt <sub>MS,3</sub>			Grt <sub>CldS,3</sub>	
<i>T</i> (°C)		590 ± 15	595 + 25/−10			585 ± 10	
<i>P</i> (GPa)		1.65 ± 0.15	1.8 + 0.05/−0.30			2.05 + 0.05/−0.40	

Note: (\*) data used for calculation (see text), the different methods are described in the manuscript.

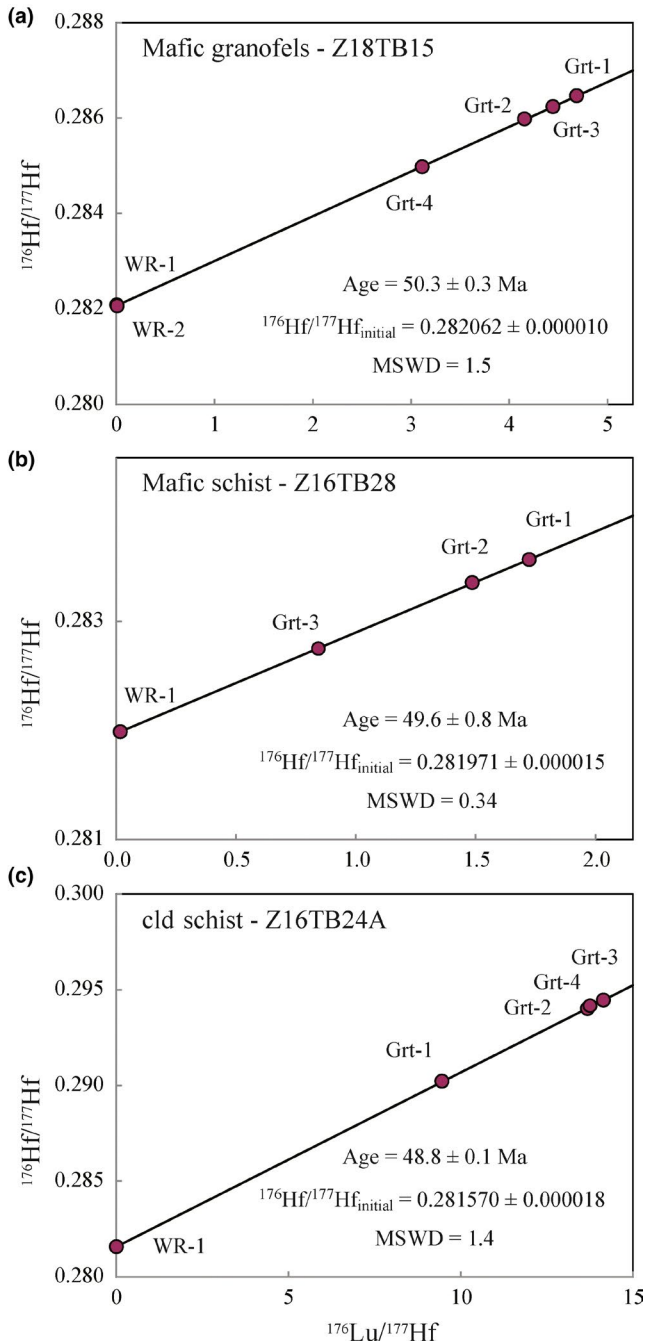


**FIGURE 12** Lu–Hf isochrones for the studied samples. (a) Mafic granofels Z18TB15. (b) Mafic schist Z16TB28. (d) Cld-schist Z16TB24A [Colour figure can be viewed at [wileyonlinelibrary.com](http://wileyonlinelibrary.com)]

mica  $P$ – $T$  conditions obtained by multi-equilibrium show similar results to the phase diagrams, with variations between samples of less than 0.5 GPa (Figure 9b,e,h) that are within the absolute uncertainty of the method ( $\pm 0.25$  GPa; Lanari & Duisterhoeft, 2019). The good agreement between  $P$ – $T$  estimates from different samples and using different thermobarometric methods—some of them not relying on the reactive bulk composition—indicates minor or insignificant chemical change for major and minor elements by metasomatism and

validates the use of bulk rock chemistry for phase equilibrium modelling in the case of pre-peak and peak- $P$  conditions.

The cores of garnet in Cld-schist Z16TB24A and mafic schist Z16TB11 are attributed to the peak- $P$  stage, and they show similar REE trends (Figure 8b,d) with minor negative Eu anomalies. The absence of plagioclase at these high- $P$  conditions and the lack of evidence for changes in oxidation state exclude these two factors as possible causes for the Eu anomaly (e.g. Ague, 2017). The weak Eu anomaly in peak- $P$  garnet is either inherited from the bulk rock (Gauthiez-Putallaz et al., 2016; Grevel et al., 2010) (Figure 8, Table S7) or due to the presence of lawsonite during prograde metamorphism (Figure 10), as confirmed by modelling and field evidence (Figure 2c). Lawsonite can have a significant positive Eu-anomaly and thus has the capacity to influence Eu budget in coexisting garnet (Hara et al., 2018; Spandler et al., 2003; Usui et al., 2007; Vitale Brovarone et al., 2014).

Post-peak metamorphic conditions are recorded in every lithology investigated (Figure 11a). These can be sub-divided further into a post-peak 1, and a post-peak 2 stage (Figures 10, 11a). Post-peak 1 is recorded by mica populations  $\text{Ph}_{\text{MS},2a}$  and  $\text{Ph}_{\text{MS},2b}$  in the mafic schists (Z16TB11 and Z16TB28), and  $\text{Ph}_{\text{CldS},2}$  in the Cld-schist (Z16TB24A). The composition of these mica populations plot in a restricted  $P$ – $T$  region at slightly lower pressure than the lawsonite-out curve (Figure 11a), at  $550 \pm 15^\circ\text{C}$  and  $2.00 \pm 0.10$  GPa with a good correspondence among phase diagram and multi-equilibrium methods (Figure 9b,e,h). Fluids are known to promote K-white mica re-equilibration (Airaghi et al., 2017; Konrad-Scholke et al., 2011). It is therefore possible that fluid released by lawsonite breakdown favoured partial K-white mica re-equilibration by replacement reactions. The lower limit of post-peak 1 conditions is constrained at  $555 \pm 15^\circ\text{C}$  and  $1.55 \pm 0.10$  GPa, as indicated by garnet from the Cld-schist ( $\text{Grt}_{\text{CldS},2}$ ; Z16TB24A) and the mafic schist ( $\text{Grt}_{\text{MS},2}$ ; Z16TB11), as well as by K-white mica from the mafic schists ( $\text{Ph}_{\text{MS},3a}$  in Z16TB11;  $\text{Ph}_{\text{MS},3b}$  in Z16TB28). Thermodynamic results for phengite for this stage coincide when comparing phase diagram and multi-equilibrium results (Figure 9e,h), except for sample Z16TB11 for which a 1 GPa discrepancy is found (Figure 9b). Post-peak 2 conditions ( $590 \pm 15^\circ\text{C}$  and  $1.70 \pm 0.10$  GPa, Figure 11a) are constrained by garnet from Cld-schist ( $\text{Grt}_{\text{CldS},3}$  in Z16TB24A), mafic schist ( $\text{Grt}_{\text{MS},3}$  in Z16TB11), and mafic granofels ( $\text{Grt}_{\text{MF},2b}$  in Z18TB15). The  $P$ – $T$  conditions are similar for  $\text{Grt}_{\text{MS},3}$  and  $\text{Grt}_{\text{MF},2b}$  at  $590 \pm 15^\circ\text{C}$  and  $1.70 \pm 0.10$  GPa, which can indicate heating from post-peak 1 if both represent a single  $P$ – $T$  cycle. The pressure stability condition of  $\text{Grt}_{\text{CldS},3}$  is  $2.05 + 0.05/-0.40$  GPa (Figure 10a,b,d), such pressure uncertainty is caused by a strong pressure dependency on minor garnet chemical variations in the model. A minimum pressure of  $\sim 1.90 \pm 0.25$  GPa is constrained by the chloritoid-in curve with  $X_{\text{Mg}}$  at 0.38 (Figure 11a). The late K-white mica

TABLE 4 Lu–Hf isotope data and apparent ages

Sample fraction	Size fraction (mm)	Concentration		Isotope ratios			Final data						
		Lu (ppm)	Hf (ppm)	$^{176}\text{Lu}/^{177}\text{Hf}$	$^{176}\text{Hf}/^{177}\text{Hf}$	2SD	Lu–Hf age (Ma)	MSWD	$^{176}\text{Hf}/^{177}\text{Hf}_{\text{initial}}$	2SD			
Grt-1	0.25–0.50	2.26	0.068	4.68700	0.0120	0.000047	0.286466	0.000047					
Grt-2	>0.50	1.82	0.062	4.15700	0.0100	0.000041	0.285977	0.000041					
Grt-3	0.25–0.50	2.31	0.074	4.44600	0.0110	0.000031	0.286234	0.000031					
Grt-4	>0.50	1.83	0.083	3.11500	0.0080	0.000037	0.284978	0.000037					
WR-1		0.336	7.26	0.006555	0.000016	0.000015	0.282081	0.000015					
WR-2		0.508	6.58	0.010954	0.000027	0.000014	0.282061	0.000014					
									All analyses included:	50.3 ± 0.3	1.5	0.282062	0.000010
Grt-1	>2.00	1.49	0.123	1.72300	0.0040	0.000026	0.283566	0.000026					
Grt-2	>2.00	1.37	0.131	1.48600	0.0040	0.000024	0.283354	0.000024					
Grt-3	>2.00	1.38	0.231	0.84580	0.0021	0.000031	0.282745	0.000031					
WR-1		0.936	7.79	0.017020	0.000040	0.000016	0.281988	0.000016					
									All analyses included:	49.6 ± 0.8	0.34	0.281971	0.000015
Grt-1	>0.50	2.52	0.038	9.45700	0.0240	0.000040	0.290219	0.000040					
Grt-2	>0.50	3.74	0.038	14.1400	0.0400	0.000043	0.294459	0.000043					
Grt-3	0.25–0.50	3.63	0.038	13.6800	0.0300	0.000044	0.294014	0.000044					
Grt-4	0.25–0.50	3.62	0.034	13.7400	0.0340	0.000050	0.294139	0.000050					
WR-1		0.444	7.96	0.007897	0.000020	0.000018	0.281576	0.000018					
									All analyses included:	48.8 ± 0.1	1.4	0.281570	0.000018

Standard deviation (SD).

generation in the mafic schist (sample Z16TB28:  $K_{wm_{MS,1}}$  and  $K_{wm_{MS,2}}$ ) cannot be modelled in the phase diagram (Figure 9e) but indicates lower pressure conditions via multi-equilibrium ( $P < 0.6$  GPa for  $T < 600^\circ\text{C}$ ).

In the mafic schist Z16TB11, garnet porphyroblasts have comparable compositions in major elements to the rim of small garnet grains (Figure 7a,b) demonstrating that large-scale equilibrium was achieved in the intergranular medium (Lanari & Engi, 2017). This implies that the garnet porphyroblasts recorded equivalent  $P$ – $T$  conditions than the small garnet rims and consequently grew during the post-peak 2 heating stage. This is supported by the thermodynamic modelling of garnet modes and compositions, which predicts significant new garnet growth at stage  $Grt_{MS,2}$  and  $Grt_{MS,3}$  (6 and 13 vol.%, respectively, Figure 10b). Additionally, the REE patterns of garnet porphyroblasts and rims of small grains have a comparable trend, without negative Eu anomalies (Figure 8a–c). This change in the europium budget could be due to lawsonite breakdown and epidote growth at this  $P$ – $T$  stage (Figure 10). There is a notable difference in HREE mass fraction, with small garnet rims being more HREE enriched than the porphyroblasts. The fine interlayering of chemical domains in the mafic schist (Figure 2c) could be the origin of the variation in REE content between garnet types, which could have grown from different local bulk compositions. The rims of garnet from Cld-schist Z16TB24A are richer in MREE than the rims of fine-grained garnet in mafic schist Z16TB11 (Figure 8b,d). This difference could reflect the presence of zoisite sequestering the MREE in the schist (Konrad-Schmolke, Zack, et al., 2008; Spandler et al., 2003).

## 6.2 | Resorption and re-equilibration of garnet

Sharp chemical zoning is observed in the small garnets from the mafic schist (Figure 4a–d) and the Cld-schist (Figure 5) and significant variations in major element are observed between garnet core and rim (Figure 7a). Garnet crystals with discontinuous chemical zoning comparable to those found in the TGU rocks have been interpreted as having recorded either a mono- or a poly-metamorphic history (Gaidies et al., 2006; Konrad-Schmolke, O'Brien, et al., 2008; Vance & O'Nions, 1990). In the Alps, most cases of poly-metamorphic garnet are reported from felsic metamorphic rocks, where Permian amphibolite to granulite facies garnet was partially overprinted by eclogite facies assemblages during Alpine subduction. Examples of similar garnet have been described in several localities including the Sesia Zone (Giuntoli, Lanari, Burn, et al., 2018; Giuntoli, Lanari, & Engi, 2018; Lanari et al., 2017), the Dent Blanche tectonic system (Manzotti et al., 2012), the Money unit in the Gran Paradiso Massif (Manzotti & Ballèvre, 2013), the Mt.

Emilius klippe (Angiboust et al., 2017; Hertgen et al., 2017), and in Corsica (Martin et al., 2011). A similar interpretation was given for poly-metamorphic garnet in mafic rocks in the Adula nappe, Central Alps (Herwartz et al., 2011; Sandmann et al., 2014). By contrast, mono-metamorphic garnet with complex internal textures was described in both mafic rocks in the Monviso unit (Angiboust et al., 2011, 2012, 2014; Locatelli et al., 2018; Rubatto & Angiboust, 2015), in the Tauern window, Eastern Alps (Kurz et al., 1998) and also postulated for felsic rocks in the Sesia Zone (Konrad-Schmolke et al., 2006). In the mono-metamorphic scenario, mechanisms invoked to explain the garnet textures were: (a) garnet fractional crystallization, (b) free fluid fractionation, (c) availability of water in the system, and (d) kinetics related to element supply required for garnet growth.

For the TGU samples, growth of garnet in different stages, as testified by the chemical zones, was investigated with series of simulations. For each simulation, equilibrium was assumed and pre-existing garnet was allowed to be preserved (fractionated) and/or resorbed. The water content required in the simulation to match the observed paragenesis was investigated prior to each modelling step, where equilibrium phase diagrams were calculated with pristine or fractionated bulk rock chemistry (Figures S7–S9). In every case, the best result was achieved with water saturation and was implemented as an input parameter in the simulation, which did not prevent development of successive garnet resorption and overgrowth steps matching the observations (Figure 10). Moreover, intracrystalline diffusion in garnet is sluggish below  $600^\circ\text{C}$  (Caddick et al., 2010) and garnet interiors are isolated from chemical equilibrium with the matrix, preventing re-equilibration (Hollister, 1966; Kohn, 2003; Spear, 1988). Consequently, interaction with an interstitial fluid, which is out of equilibrium with pre-existing garnet in a water-saturated system is the best candidate to trigger mineral reactions and mineral re-equilibration with changing  $P$ – $T$  conditions (Ferry, 1983; Putnis, 2009). The  $P$ – $T$  conditions of K-white mica re-equilibration by dissolution–precipitation, together with the results of thermodynamic modelling on garnet constrained fluid–rock interaction to happen during the first stage of decompression at  $\sim 560 \pm 10^\circ\text{C}$  and  $1.9 \pm 0.1$  GPa (Figure 11a).

One possibility for the release of fluids and consequent fluid–rock interaction is lawsonite dehydration, as the lawsonite out curve is crossed during the exhumation path (Figure 11a). Because lawsonite contains 11–12 wt%  $\text{H}_2\text{O}$  (Okamoto & Maruyama, 1999; Poli & Schmidt, 2002), this dehydration reaction can lead to significant water release during retrogression, as described for other metaophiolites of the western Alps (Angiboust & Agard, 2010; Angiboust et al., 2012; Groppo et al., 2009; Reinecke, 1998; Vitale Brovarone & Beysac, 2014). In the investigated rock types, lawsonite is predicted to be stable at pressure peak conditions (Figure 10a–c) with varying modal abundance: 26 vol.% in

mafic granulites (Z16TB32), 22% in mafic schist (Z16TB11), and 1% in Cld-schist (Z16TB24A). Forward modelling using Theriak Domino simulating an isothermal decompression from the pressure peak (580°C, 2.65 GPa) to the post-peak 1 conditions (555°C, 1.55 GPa), shows variable amount of water release associated with hydrous mineral breakdown: ~0.5 wt% water release in the Cld-schist due to successive carpholite and lawsonite breakdown; ~1.5 wt% water release in the mafic schist, where Lws-out reaction produces zoisite; ~2.5 wt% water release in the mafic granulites, where lawsonite is replaced by zoisite and quartz (Figure S11). These values are above the threshold for pore connectivity (2 vol.%) that allows water migration in eclogite (Mibe et al., 2003) and will likely saturate the system in H<sub>2</sub>O. These fluids may have circulated along preferential pathways within and across samples, such as in the garnet-rich zone in the mafic schist, where most grains have complex replacement textures.

Based on field observations and a detailed petrological study, we identified structures indicating intense deformation, such as mafic boudin stretched within the schists and veinlets with high-*P* assemblage (almandine–grossular and diopside) cross cutting the mafic granulites (Figure 2a and Figure S12a). Additionally, some schist layers contain abundant deformed clusters of garnet grains that show replacement textures, and which could be interpreted as brittle deformation of garnet in shear zones (Figure S12b). These features are comparable to what described for the high-*P* shear zones within the Monviso eclogites, and that have been linked to ductile shearing, brittle failure and fluid–rock interaction (Angiboust, Agard, et al., 2012; Locatelli et al., 2018, 2019). Also in the case of the TGU it is possible that the garnet microtextures are indicative of fluid pulses linked to seismic brecciation and intermediate-depth earthquakes.

### 6.3 | Garnet and the mono-metamorphic nature of the TGU

The *P–T* evolution of the TGU reconstructed so far could represent a single cycle of burial and exhumation. Determining this issue with certainty—and interpreting the *P–T* data in terms of tectonic and geodynamic processes—may prove to be difficult on the basis of *P–T* data alone. Garnet geochronology provides absolute age constraints needed to solve the mono- versus poly-metamorphic character of the TGU, as it has been shown in other studies in the Alps with similar complex garnet chemical zoning (Herwartz et al., 2011; Sandmann et al., 2014). In this study, the three dated samples yield similar Lu–Hf age between  $50.3 \pm 0.3$  and  $48.8 \pm 0.1$  Ma. In each sample the initial  $^{176}\text{Hf}/^{177}\text{Hf}$  is lower than the CHUR value as expected for crustal samples. Notably, there is no resolvable age difference between sample Z16TB24A, which contains garnet with complex textures and sharp chemical

transition between core and rim, and samples where garnet shows continuous single-stage growth zoning (Z16TB28 and Z18TB15). It is unlikely that these ages are significantly influenced by diffusional re-equilibration of either Lu or Hf. Lutetium distributions show sharp and euhedral zoning and even fine oscillations, indicating primary HREE growth zoning is preserved and diffusional re-equilibration did not occur on scales larger than microns. Given that diffusivity of Hf<sup>4+</sup> in garnet is even slower than that of Lu<sup>3+</sup> (Bloch et al., 2015; Ganguly & Tirone, 1999), we interpret the Lu–Hf ages as each reflecting garnet growth during the Alpine metamorphic history of the tectonic unit. These results confirm that the lithologies of the TGU underwent a single Alpine metamorphic cycle with early garnet growth at 50–49 Ma.

Garnet porphyroblasts from the mafic schist (Z16TB11), used for GrtMod thermodynamic modelling, has the highest Lu concentration in the garnet core, whereas the rim is characterized by oscillatory and sector zoning (Figure 6b). The dated garnet porphyroblasts in the mafic schist (Z16TB28) present similar major element compositions (Figure 7b) and similar REE core to rim patterns (Figure 8a,c). In both mafic schist samples (Z16TB11 and Z16TB28), garnet porphyroblasts show HREE-depleted rims compared to their core (Figure 8a,b), possibly reflecting Rayleigh fractionation of elements that are compatible in garnet (Moore et al., 2013; Otamendi et al., 2002). We interpret the Lu distribution in Z16TB11 as representative for the dated sample Z16TB28.

As discussed above, garnet in these samples records complex zoning that represents a substantial range of *P–T* conditions and thus a time span. In a bulk-grain garnet analysis, and in the absence of diffusional re-equilibration of Lu and Hf, the Lu–Hf age may be biased towards zones that contribute most to the bulk-grain Lu budget (e.g. Lapen et al., 2003; Smit et al., 2010). Garnet in all samples investigated shows Lu-enriched cores and thus the Lu–Hf ages in these samples can be generally taken to represent the early stage of garnet growth, as is common in eclogite facies garnet (Lapen et al., 2003; Skora et al., 2006; Smit et al., 2010). Therefore, the Lu zoning in each garnet type (Figure 6) can further assist in assigning the age to a particular *P–T* stage. The three Lu–Hf ages are different outside analytical uncertainty. GrtMod thermodynamic models indicate that garnet from the mafic granulites records the early stage of TGU metamorphism. This garnet type yields the oldest age ( $50.3 \pm 0.3$  Ma), probably representing the initiation of TGU prograde metamorphism. The Lu-rich core of garnet with sharp chemical zoning from the Cld-schists is predicted stable at maximum metamorphic pressure, which consequently occurred *c.* 1.5 Ma later at  $48.8 \pm 0.1$  Ma. Finally, major element and REE composition of garnet porphyroblasts from the mafic schist indicate growth during the re-heating stage. The garnet porphyroblasts yielded an age of  $49.6 \pm 0.8$  Ma, which is within uncertainty

of the age of the small garnet and thus argues for rapid initial decompression and exhumation, within 1 Ma.

The ages obtained for Alpine metamorphism in this study are consistent with what was determined with various dating methods for Alpine metamorphism in the surrounding metaophiolites from the Western Alps: 52–40 Ma for eclogites from ZSZ on the basis of zircon and garnet dating (Amato et al., 1999; Dragovic et al., 2020; Lapen et al., 2003; Meyer et al., 2014; Rubatto et al., 1998; Skora et al., 2015), as well as Rb–Sr geochronology of mica inclusions in garnet (De Meyer et al., 2014). Comparable ages are recorded in the Monviso metaophiolite, which underwent a similar  $P$ – $T$  evolution during Alpine subduction:  $49.2 \pm 1.2$  Ma for garnet (Duchêne et al., 1997), and 46–45 Ma for high- $P$  zircon rims in eclogites (Rubatto & Angiboust, 2015; Rubatto & Hermann, 2003). Garnet from eclogites from the continental slice of Etirol-Levaz yielded older ages of  $61.8 \pm 1.8$  Ma and  $52.4 \pm 2.1$  Ma, which could indicate a different timing of subduction-related metamorphism in this sub-units (Fassmer et al., 2016). High- $P$  zircon in an eclogite from the Etirol-Levaz unit was dated at  $47.5 \pm 1.0$  Ma, in agreement with other metaophiolite slices (Beltrando et al., 2010). Moreover, the 50–49 Ma Lu–Hf garnet ages obtained for all lithologies in this study are slightly younger than the Lu–Hf garnet ages described by Weber et al. (2015) from garnet in mafic granofels ( $56.5 \pm 2.7$  Ma and  $58.2 \pm 1.4$  Ma) and favours a synchronous  $P$ – $T$  path between TGU and ZSZ unit during Eocene.

#### 6.4 | Geothermal gradient and comparison with surrounding tectonic units

The recognition of the  $P$ – $T$ –time data as representing a single metamorphic cycle enables interpretation of these data in terms of tectonic and geodynamic processes. The  $P$ – $T$ –time path of the TGU is characterized by two metamorphic maxima occurring at approximately the same temperature but at significantly different pressures (Figure 11a). Thermal structure fluctuations in subduction zones could either be linked to the thermal structure of the lithosphere itself (Peacock & Wang, 1999), to variation in the rate of subduction (Peacock & Wang, 1999), or to endothermic reactions in the subducting lithologies (Reinecke, 1998). The prograde  $P$ – $T$  path is characterized by a steep increase in pressure of  $\sim 1$  GPa over  $\sim 90^\circ\text{C}$  (Figure 11b), indicating rapid burial with only minor thermal equilibration. The maximum  $P$ – $T$  conditions lie on a cold apparent geotherm of  $\sim 6^\circ\text{C}/\text{km}$  expected for rapid burial of cold surface sediments (Philpotts & Ague, 2009). This prograde-to-peak evolution is comparable to what was previously reported for tectonic units in the same region in the Western Alps (Figure 11b), for example, ZSZ (Angiboust et al., 2009; Bucher et al., 2005; Groppo et al., 2009; Reinecke, 1998),

Etirol-Levaz Unit (Fassmer et al., 2016), and Monviso (Angiboust, Langdon, et al., 2012). In these units, peak metamorphism is followed by isothermal decompression, for example, ZSZ in Pfulwe (Bucher et al., 2005), Lago di Cignana (Reinecke, 1998), and Täschalp (Barnicoat & Fry, 1986) and for some continental outliers (Angiboust et al., 2017; Fassmer et al., 2016). Such  $P$ – $T$  trajectory is possible if the tectonic units follow a rapid exhumation after decoupling from the descending slab (Philpotts & Ague, 2009; Rubatto & Hermann, 2001). Numerical simulations that report pressure and temperature pathways of rocks during collision and subsequent exhumation correlate an isothermal pressure drop with the onset of slab break off (Vogt & Gerya, 2014), which may be the geodynamic process governing initial exhumation of the TGU as well.

After a first stage of near isothermal decompression (post-peak 1), the exhumation path of the TGU reflects a minor, almost isobaric, heating episode lying on a slightly hotter geotherm of  $\sim 10^\circ\text{C}/\text{km}$  (post-peak 2). The apparent pressure increase between post-peak 1 and post-peak 2 is not considered significant, since it is only constrained by the chloritoid isopleth, which could also reflect minor inconsistencies in the thermodynamic data. The  $\beta$ -shaped  $P$ – $T$  path for TGU is consistent with the exhumation paths proposed for the ZSZ (Figure 11b; e.g. Angiboust et al., 2009; Bucher et al., 2005). Similar  $\beta$ -shaped  $P$ – $T$  paths have been reported for many orogens indicating that thermal pulses during exhumation are potentially a common feature. Examples of  $\beta$ -shaped  $P$ – $T$  paths are reported for many HP terranes worldwide (Faryad et al., 2019; Gao et al., 2011; O'Brien, 2000; Whitney et al., 2011; Wilke et al., 2010), including the Tauern window in the Eastern Alps (e.g. Kurz et al., 2008; Ratschbacher et al., 2004), the Lepontine Dome in the Central Alps (Wiederkehr et al., 2008), the Internal Penninic Nappes in the Western Alps (e.g. Borghi et al., 1996; Brouwer et al., 2002; Rubatto & Hermann, 2001), and the Upper Penninic Nappes in the Western Alps (Beltrando et al., 2007; Messiga & Scambelluri, 1991). Various mechanisms have been invoked to affect geothermal gradient and explain the subsequent reheating step, such as radiogenic heat production of additionally accreted continental blocks (Wiederkehr et al., 2008), slab breakoff (Brouwer et al., 2002; Kurz et al., 1998), continental collision after the end of oceanic lithosphere subduction (Borghi et al., 1996), mantle delamination (Henk et al., 2000), slowing exhumation rate (e.g. Wilke et al., 2010), asthenospheric inflow ahead of the spreading ridge (Abers et al., 2016), transient storage at MOHO depth during exhumation (Walsh & Hacker, 2004) and multiple, short-lived burial-exhumation cycles related to orogen-scale switches between shortening and extensional deformation (Beltrando et al., 2007). Recent numerical modelling of exhumation mechanisms has identified advective and conductive heating from the mantle, rather than radiogenic or shear heating, as

best candidates to explain rapid (short-lived) heating of rocks during exhumation (Sizova et al., 2019). The numerical results show  $\beta$ -shaped  $P$ - $T$ -time paths with re-heating of up to 200°C at various pressure (0.5–1.5 GPa) and involve asthenospheric upwelling related to slab rollback or slab bending, or crustal exhumation paired with slab breakoff, as prime driver for late orogenic heating during exhumation (Sizova et al., 2019). In the case of the TGU, the imprint of such processes would be relatively strong, as this unit is structurally located on top of the subducted oceanic crust and is therefore located closest to the slab-mantle interface where thermal anomalies would be most intense.

## 6.5 | Comparison with previous findings

Complex garnet textures with sharp chemical zoning in the TGU were previously interpreted as the result of polycyclic metamorphism (Bucher et al., 2019). The garnet zoning of the schist samples investigated in this study (Z16TB11 and Z16TB24A) shows good correspondence with those observed by Bucher et al. (2019). In both cases, a marked compositional difference is present between garnet core and rim (Figure 7a). However, in this study Lu–Hf geochronological data obtained for garnet from different lithologies returned coherent Alpine ages in every sample. Particularly, the Alpine age of Cld-schist (Z16TB24A), where garnet has a discontinuous core–rim zoning, excludes a pre-Alpine (Permian) metamorphic stage as suggested by Bucher et al. (2019). This study demonstrates that such textural record is compatible with a mono-metamorphic evolution of the TGU. As a main consequence, there is no longer discrepancy for the TGU Alpine peak  $P$ - $T$  conditions between the mafic granofels at  $2.2 \pm 0.1$  GPa and  $580 \pm 50^\circ\text{C}$  (Weber & Bucher, 2015), and the schist at  $\sim 1.7$  GPa and  $\sim 530^\circ\text{C}$  (Bucher et al., 2019). The garnet core in the schists (granulitic according to Bucher et al., 2019) is re-interpreted as representing Alpine peak- $P$  conditions, corresponding to the maximum  $P$ - $T$  conditions inferred in the TGU mafic granofels at  $2.65 \pm 0.10$  GPa and  $580 \pm 15^\circ\text{C}$  (this study; Weber & Bucher, 2015). Likewise, the maximum  $P$ - $T$  conditions for the metapelites in Bucher et al. (2019) corresponds to the initiation of the re-heating stage after the first step of exhumation, rather than the Alpine peak pressure for these rocks.

Compositional maps of the garnet in the Cld-schist (Z16TB24A) (Figure 4a–d) and the matrix garnet of the mafic schist (Z16TB11) (Figure 5) show a sharp chemical boundary in major elements between core and rim at the high lateral resolution of the EMPA map ( $\sim 1$   $\mu\text{m}$  in garnet, see Lanari & Piccoli, 2020). Pristine chemical zoning could be modified by diffusional relaxation, which is dependent on cooling rate and grain size (Dodson, 1973), because there is a strong dependence between cation diffusivity and temperature in

minerals (Caddick et al., 2010). The sharp zoning shows no evidence of diffusional re-equilibration of relatively fast diffusing divalent cations at sharp chemical interfaces in garnet, such as Fe, Mg, and Mn (Carlson, 2006; Li et al., 2018; Perchuk et al., 2009). This result is inconsistent with the interpretation that the TGU resided at 530–580°C for *c.* 10 Ma (Bucher et al., 2019), but rather argue for a fast  $P$ - $T$  cycle as suggested by our Lu–Hf data.

## 7 | CONCLUSIONS

The  $P$ - $T$  path reconstructed for the TGU unit combined with Lu–Hf dating of garnet reveals a coherent mono-metamorphic history during Eocene, which is in agreement with the surrounding ZSZ metaophiolites. After a first stage of decompression, the exhumation path of the TGU records a reheating event. Complex garnet textures are thus reconciled with a mono-metamorphic evolution and a  $\beta$ -shaped  $P$ - $T$  path. The thermal pulse is best explained by upwelling of hot asthenospheric mantle, favoured by the structural position of the TGU located atop of the subducted oceanic crust and therefore closer to the slab-mantle interface. During exhumation of the TGU, lawsonite dehydration occurring in both the mafic schist and the mafic granofels is a main fluid source for fluid–rock interaction at high pressure. The presence of significant amounts of fluids leads to complex texture development in garnet from the schist, K-white mica re-equilibration in the schists and vein formation in the mafic granofels.

## ACKNOWLEDGEMENT

We are grateful to J. Hermann and T. Ewing for constructive discussion. We thank D. Peters and J. Cutts for their help with the laboratory work. Further thanks go to D. Moynihan, T. G. Lee, J. Reynes and E. Kempf for their assistance during fieldwork. This work was supported by the Swiss National Science Foundation (Project N. 200021\_166280 D. Rubatto and 206021\_170722 to D. Rubatto and T. Pettke). We thank Stéphanie Duchêne, Besim Dragovic and an anonymous reviewer for their insightful comments that helped to improve the quality of this manuscript, and Julia Baldwin and Richard White for editorial handling.

## ORCID

Thomas Bovay  <https://orcid.org/0000-0002-3508-238X>

Pierre Lanari  <https://orcid.org/0000-0001-8303-0771>

Daniela Rubatto  <https://orcid.org/0000-0002-7425-7904>

## REFERENCES

- Abers, G. A., Eilon, Z., Gaherty, J. B., Jin, G., Kim, Y., Obrebski, M., & Dieck, C. (2016). Southeast Papuan crustal tectonics: Imaging extension and buoyancy of an active rift. *Journal of*

- Geophysical Research: Solid Earth*, 121(2), 951–971. <https://doi.org/10.1002/2015JB012621>
- Ague, J. J. (2017). Element mobility during regional metamorphism in crustal and subduction zone environments with a focus on the rare earth elements (REE). *American Mineralogist*, 102(9), 1796–1821. <https://doi.org/10.2138/am-2017-6130>
- Airaghi, L., Lanari, P., de Sigoyer, J., & Guillot, S. (2017). Microstructural vs compositional preservation and pseudomorphic replacement of muscovite in deformed metapelites from the Longmen Shan (Sichuan, China). *Lithos*, 282–283, 262–280. <https://doi.org/10.1016/j.lithos.2017.03.013>
- Amato, J. M., Johnson, C. M., Baumgartner, L. P., & Beard, B. L. (1999). Rapid exhumation of the Zermatt-Saas ophiolite deduced from. *Earth and Planetary Science Letters*, 171, 425–438.
- Angiboust, S., & Agard, P. (2010). Lithos Initial water budget: The key to detaching large volumes of eclogitized oceanic crust along the subduction channel ? *Lithos*, 120(3–4), 453–474. <https://doi.org/10.1016/j.lithos.2010.09.007>
- Angiboust, S., Agard, P., Jolivet, L., & Beyssac, O. (2009). The Zermatt-Saas ophiolite: The largest (60-km wide) and deepest (c. 70–80km) continuous slice of oceanic lithosphere detached from a subduction zone? *Terra Nova*. <https://doi.org/10.1111/j.1365-3121.2009.00870.x>
- Angiboust, S., Agard, P., Raimbourg, H., Yamato, P., & Huet, B. (2011). Subduction interface processes recorded by eclogite-facies shear zones (Monviso, W. Alps). *Lithos*, 127(1–2), 222–238. <https://doi.org/10.1016/j.lithos.2011.09.004>
- Angiboust, S., Agard, P., Yamato, P., & Raimbourg, H. (2012). Eclogite breccias in a subducted ophiolite: A record of intermediate depth earthquakes? *Geology*, 40(8), 707–710. <https://doi.org/10.1130/G32925.1>
- Angiboust, S., Langdon, R., Agard, P., Waters, D., & Chopin, C. (2012). Eclogitization of the Monviso ophiolite (W. Alps) and implications on subduction dynamics. *Journal of Metamorphic Geology*, 30(1), 37–61. <https://doi.org/10.1111/j.1525-1314.2011.00951.x>
- Angiboust, S., Pettke, T., De Hoog, J. C. M., Caron, B., & Oncken, O. (2014). Channelized fluid flow and eclogite-facies metasomatism along the subduction shear zone. *Journal of Petrology*, 55(5), 883–916. <https://doi.org/10.1093/ptrology/egu010>
- Angiboust, S., Yamato, P., Hertgen, S., Hyppolito, T., Bebout, G. E., & Morales, L. (2017). Fluid pathways and high-P metasomatism in a subducted continental slice (Mt. Emilius klippe, W. Alps). *Journal of Metamorphic Geology*, 35(5), 471–492. <https://doi.org/10.1111/jmg.12241>
- Ballèvre, M., Kienast, J.-R., & Vuichard, J.-P. (1986). La “nappe de la Dent blanche” (Alpes occidentales): Deux unités austroalpines indépendantes. *Eclogae Geologicae Helveticae*, 79(1), 57–74.
- Barnicoat, A. C., & Fry, N. (1986). High-pressure metamorphism of the Zermatt-Saas ophiolite zone, Switzerland. *Journal of the Geological Society*, 143(4), 607–618. <https://doi.org/10.1144/gsjgs.143.4.0607>
- Baxter, E. F., Caddick, M. J., & Ague, J. J. (2013). Garnet: Common mineral, uncommonly useful. *Elements*, 9(6), 415–419. <https://doi.org/10.2113/gselements.9.6.415>
- Baxter, E. F., Caddick, M. J., & Dragovic, B. (2017). Garnet: A rock-forming mineral petrochronometer. *Reviews in Mineralogy and Geochemistry*, 83(1), 469–533. <https://doi.org/10.2138/rmg.2017.83.15>
- Bearth, P. (1967). Die ophiolite der Zone von Zermatt-Saas Fee. *Beiträge Geologische Karte Schweiz*, 132, 1–130.
- Beltrando, M., Hermann, J., Lister, G., & Compagnoni, R. (2007). On the evolution of orogens: Pressure cycles and deformation mode switches. *Earth and Planetary Science Letters*, 256(3–4), 372–388. <https://doi.org/10.1016/j.epsl.2007.01.022>
- Beltrando, M., Manatschal, G., Mohn, G., Dal Piaz, G. V., Vitale Brovarone, A., & Masini, E. (2014). Recognizing remnants of magma-poor rifted margins in high-pressure orogenic belts: The Alpine case study. *Earth-Science Reviews*, 131, 88–115. <https://doi.org/10.1016/j.earscirev.2014.01.001>
- Beltrando, M., Rubatto, D., & Manatschal, G. (2010). From passive margins to orogens: The link between ocean-continent transition zones and (ultra)high-pressure metamorphism. *Geology*, 38(6), 559–562. <https://doi.org/10.1130/G30768.1>
- Bizzarro, M., Baker, J. A., & Ulfbeck, D. (2003). A new digestion and chemical separation technique for rapid and highly reproducible determination of Lu/Hf and Hf isotope ratios in geological materials by mc-ICP-MS. *Geostandards Newsletter*, 27(2), 133–145. <https://doi.org/10.1111/j.1751-908X.2003.tb00641.x>
- Blichert-Toft, J., Boyet, M., Télouk, P., & Albarède, F. (2002). <sup>147</sup>Sm-<sup>143</sup>Nd and <sup>176</sup>Lu-<sup>176</sup>Hf in eucrites and the differentiation of the HED parent body. *Earth and Planetary Science Letters*, 204(1–2), 167–181. [https://doi.org/10.1016/S0012-821X\(02\)00976-7](https://doi.org/10.1016/S0012-821X(02)00976-7)
- Blichert-Toft, J., Chauvel, C., & Albarède, F. (1997). Separation of Hf and Lu for high-precision isotope analysis of rock samples by magnetic sector-multiple collector ICP-MS. *Contributions to Mineralogy and Petrology*, 127, 248–260. <https://doi.org/10.1007/s004100050278>
- Bloch, E., Ganguly, J., Hervig, R., & Cheng, W. (2015). <sup>176</sup>Lu-<sup>176</sup>Hf geochronology of garnet I: Experimental determination of the diffusion kinetics of Lu<sup>3+</sup> and Hf<sup>4+</sup> in garnet, closure temperatures and geochronological implications. *Contributions to Mineralogy and Petrology*, 169(2), <https://doi.org/10.1007/s00410-015-1109-8>
- Borghi, A., Compagnoni, R., & Sandrone, R. (1996). Composite P-T paths in the Internal Penninic Massifs of the Western Alps: Petrological constraints to their thermo-mechanical evolution. *Eclogae Geologicae Helveticae*, 89(1), 345–367.
- Bousquet, R., Oberhänsli, R., Goffé, B., Wiederkehr, M., Koller, F., Schmid, S. M., Schuster, R., Engi, M., Berger, A., & Martinotti, G. (2008). Metamorphism of metasediments at the scale of an orogen: A key to the Tertiary geodynamic evolution of the Alps. *Geological Society, London, Special Publications*, 298(1), 393–411. <https://doi.org/10.1144/SP298.18>
- Bovay, T. (2021). *Origin and pressure-temperature-time-fluid evolution of a subducted volcanoclastic sequence: The Theodul Glacier Unit (Western Alps, Switzerland)*. University of Bern.
- Bovay, T., Rubatto, D., & Lanari, P. (2021). Pervasive fluid-rock interaction in subducted oceanic crust revealed by oxygen isotope zoning in garnet. *Contributions to Mineralogy and Petrology*, 176, 55. <https://doi.org/10.1007/s00410-021-01806-4>
- Brouwer, F. M., Vissers, R. L. M., & Lamb, W. M. (2002). Structure and metamorphism of the Gran Paradiso massif, western Alps, Italy. *Contributions to Mineralogy and Petrology*, 143(4), 450–470. <https://doi.org/10.1007/s00410-002-0357-6>
- Bucher, K., Fazis, Y., de Capitani, C., & Grapes, R. (2005). Blueschists, eclogites, and decompression assemblages of the Zermatt-Saas ophiolite: High-pressure metamorphism of subducted Tethys lithosphere. *American Mineralogist*, 90(5–6), 821–835. <https://doi.org/10.2138/am.2005.1718>
- Bucher, K., Weisenberger, T. B., Klemm, O., & Weber, S. (2019). Decoding the complex internal chemical structure of garnet

- porphyroblasts from the Zermatt area, Western Alps. *Journal of Metamorphic Geology*, 37(9), 1151–1169. <https://doi.org/10.1111/jmg.12506>
- Bucher, K., Weisenberger, T. B., Weber, S., Klemm, O., & Corfu, F. (2020). The Theodul Glacier Unit, a slab of pre-Alpine rocks in the Alpine meta-ophiolite of Zermatt-Saas, Western Alps. *Swiss Journal of Geosciences*, 113(1), 1–22. <https://doi.org/10.1186/s00015-020-00354-6>
- Caddick, M. J., Konopásek, J., & Thompson, A. B. (2010). Preservation of garnet growth zoning and the duration of prograde metamorphism. *Journal of Petrology*, 51(11), 2327–2347. <https://doi.org/10.1093/ptrology/egq059>
- Carlson, W. D. (2006). Rates of Fe, Mg, Mn, and Ca diffusion in garnet. *American Mineralogist*, 91(1), 1–11. <https://doi.org/10.2138/am.2006.2043>
- Coggon, R., & Holland, T. J. B. (2002). Mixing properties of phengitic micas and revised garnet-phengite thermobarometers. *Journal of Metamorphic Geology*, 20(7), 683–696. <https://doi.org/10.1046/j.1525-1314.2002.00395.x>
- Compagnoni, R. (1977). The Sesia-Lanzo Zone: High pressure-low temperature metamorphism in the Austroalpine continental margin. *Rendiconti Della Società Italiana Di Mineralogia E Petrologia*, 33(1), 335–374.
- Cotta, A. J. B., Enzweiler, J., Wilson, S. A., Pérez, C. A., Nardy, A. J. R., & Larizzatti, J. H. (2007). Homogeneity of the geochemical reference material BRP-1 (paranábasin basalt) and assessment of minimum mass. *Geostandards and Geoanalytical Research*, 31(4), 379–393. <https://doi.org/10.1111/j.1751-908X.2007.00111.x>
- Dal Piaz, G. V. (1979). Manganiferous quartzitic schists of the Piemonte ophiolite nappe in the Valsesia-Valtournanche area (Italian Western Alps). *Memorie degli Istituti di geologia e mineralogia dell'Università di*, 32, 1–24. <https://ci.nii.ac.jp/naid/10003418574/en/>
- Dal Piaz, G. V. (2001). History of tectonic interpretations of the Alps. *Journal of Geodynamics*, 32(1–2), 99–114. [https://doi.org/10.1016/S0264-3707\(01\)00019-9](https://doi.org/10.1016/S0264-3707(01)00019-9)
- Dal Piaz, G. V., Cortiana, G., Del Moro, A., Martin, S., Pennacchioni, G., & Tartarotti, P. (2001). Tertiary age and paleostructural inferences of the eclogitic imprint in the Austroalpine outliers and zermatt-saas ophiolite, Western Alps. *International Journal of Earth Sciences*, 90(3), 668–684. <https://doi.org/10.1007/s005310000177>
- Dal Piaz, G. V., & Ernst, W. G. (1978). Areal geology and petrology of eclogites and associated metabasites of the Piemonte ophiolite nappe, breuil-st. Jacques area, Italian Western Alps. *Tectonophysics*, 51(1–2), 99–126. [https://doi.org/10.1016/0040-1951\(78\)90053-7](https://doi.org/10.1016/0040-1951(78)90053-7)
- De Capitani, C., & Brown, T. H. (1987). The computation of chemical equilibrium in complex systems containing non-ideal solutions. *Geochimica et Cosmochimica Acta*, 51, 2639–2652. [https://doi.org/10.1016/0016-7037\(87\)90145-1](https://doi.org/10.1016/0016-7037(87)90145-1)
- De Capitani, C., & Petrakakis, K. (2010). The computation of equilibrium assemblage diagrams with Theriak/Domino software. *American Mineralogist*, 95(7), 1006–1016. <https://doi.org/10.2138/am.2010.3354>
- De Meyer, C. M. C., Baumgartner, L. P., Beard, B. L., & Johnson, C. M. (2014). Rb-Sr ages from phengite inclusions in garnets from high pressure rocks of the swiss western Alps. *Earth and Planetary Science Letters*, 395, 205–216. <https://doi.org/10.1016/j.epsl.2014.03.050>
- Diener, J. F. A., Powell, R., White, R. W., & Holland, T. J. B. (2007). A new thermodynamic model for clino- and orthoamphiboles in the system Na<sub>2</sub>O-CaO-FeO-MgO-Al<sub>2</sub>O<sub>3</sub>-SiO<sub>2</sub>-H<sub>2</sub>O-O. *Journal of Metamorphic Geology*, 25(6), 631–656. <https://doi.org/10.1111/j.1525-1314.2007.00720.x>
- Dilek, Y., & Furnes, H. (2014). Ophiolites and their origins. *Elements*, 10(2), 93–100. <https://doi.org/10.2113/gselements.10.2.93>
- Dodson, M. H. (1973). Closure temperature in cooling geochronological and petrological systems. *Contributions to Mineralogy and Petrology*, 40(3), 259–274. <https://doi.org/10.1007/BF00373790>
- Dragovic, B., Angiboust, S., & Tappa, M. J. (2020). Petrochronological close-up on the thermal structure of a paleo-subduction zone (W. Alps). *Earth and Planetary Science Letters*, 547. <https://doi.org/10.1016/j.epsl.2020.116446>
- Dubacq, B., Vidal, O., & de Andrade, V. (2010). Dehydration of dioctahedral aluminous phyllosilicates: Thermodynamic modelling and implications for thermobarometric estimates. *Contributions to Mineralogy and Petrology*, 159(2), 159–174. <https://doi.org/10.1007/s00410-009-0421-6>
- Duchêne, S., Blichert-Toft, J., Luais, B., Télouk, P., Lardeaux, J. M., & Albarède, F. (1997). The Lu-Hf dating of garnets and the ages of the Alpine high-pressure metamorphism. *Nature*, 387(6633), 586–589. <https://doi.org/10.1038/42446>
- Escher, A., Hunziker, J.-C., Marthaler, M., Masson, H., Sartori, M., & Steck, A. (1997). Geologic framework and structural evolution of the western Swiss-Italian Alps. In O. A. Pfiffner, P. Lehner, P. Heitzmann, S. Mueller, & A. Steck (Eds.), *Deep structure of the Swiss Alps: Results of NRP* (vol. 20, pp. 205–221). Birkhäuser Verlag.
- Evans, T. P. (2004). A method for calculating effective bulk composition modification due to crystal fractionation in garnet-bearing schist: Implications for isopleth thermobarometry. *Journal of Metamorphic Geology*, 22(6), 547–557. <https://doi.org/10.1111/j.1525-1314.2004.00532.x>
- Faryad, S. W., Baldwin, S. L., Jedlicka, R., & Ježek, J. (2019). Two-stage garnet growth in coesite eclogite from the southeastern Papua New Guinea (U)HP terrane and its geodynamic significance. *Contributions to Mineralogy and Petrology*, 174(9), 1–16. <https://doi.org/10.1007/s00410-019-1612-4>
- Fassmer, K., Obermüller, G., Nagel, T. J., Kirst, F., Froitzheim, N., Sandmann, S., Miladinova, I., Fonseca, R. O. C., & Münker, C. (2016). High-pressure metamorphic age and significance of eclogite-facies continental fragments associated with oceanic lithosphere in the Western Alps (Etirol-Levaz Slice, Valtournanche, Italy). *Lithos*, 252–253, 145–159. <https://doi.org/10.1016/j.lithos.2016.02.019>
- Feenstra, A., Petrakakis, K., & Rhede, D. (2007). Variscan relicts in Alpine high-P pelitic rocks from Samos (Greece): Evidence from multi-stage garnet and its included minerals. *Journal of Metamorphic Geology*, 25(9), 1011–1033. <https://doi.org/10.1111/j.1525-1314.2007.00741.x>
- Ferry, J. M. (1983). On the control of temperature, fluid composition, and reaction progress during metamorphism. *American Journal of Science*, 283-A, 201–232.
- Gaidies, F., Abart, R., De Capitani, C., Schuster, R., Connolly, J. A. D., & Reusser, E. (2006). Characterization of polymetamorphism in the Austroalpine basement east of the Tauern Window using garnet isopleth thermobarometry. *Journal of Metamorphic Geology*, 24(6), 451–475. <https://doi.org/10.1111/j.1525-1314.2006.00648.x>
- Ganguly, J., & Tirone, M. (1999). Diffusion closure temperature and age of a mineral with arbitrary extent of diffusion: Theoretical formulation and applications. *Earth and Planetary Science Letters*, 170(1–2), 131–140. [https://doi.org/10.1016/S0012-821X\(99\)00089-8](https://doi.org/10.1016/S0012-821X(99)00089-8)

- Gao, X. Y., Zheng, Y. F., & Chen, Y. X. (2011). U-Pb ages and trace elements in metamorphic zircon and titanite from UHP eclogite in the Dabie orogen: Constraints on P-T-t path. *Journal of Metamorphic Geology*, 29(7), 721–740. <https://doi.org/10.1111/j.1525-1314.2011.00938.x>
- Gauthiez-Putallaz, L., Rubatto, D., & Hermann, J. (2016). Dating prograde fluid pulses during subduction by in situ U-Pb and oxygen isotope analysis. *Contributions to Mineralogy and Petrology*, 171(2), 1–20. <https://doi.org/10.1007/s00410-015-1226-4>
- George, F. R., Gaidies, F., & Boucher, B. (2018). Population-wide garnet growth zoning revealed by LA-ICP-MS mapping: Implications for trace element equilibration and syn-kinematic deformation during crystallisation. *Contributions to Mineralogy and Petrology*, 173(9), 1–22. <https://doi.org/10.1007/s00410-018-1503-0>
- Giuntoli, F., Lanari, P., Burn, M., Eva Kunz, B., & Engi, M. (2018). Deeply subducted continental fragments – Part 2: Insight from petrochronology in the central Sesia Zone (western Italian Alps). *Solid Earth*, 9(1), 191–222. <https://doi.org/10.5194/se-9-191-2018>
- Giuntoli, F., Lanari, P., & Engi, M. (2018). Deeply subducted continental fragments – Part 1: Fracturing, dissolution-precipitation, and diffusion processes recorded by garnet textures of the central Sesia Zone (western Italian Alps). *Solid Earth*, 9(1), 167–189. <https://doi.org/10.5194/se-9-167-2018>
- Green, E., Holland, T., & Powell, R. (2007). An order-disorder model for omphacitic pyroxenes in the system jadeite-diopside-hedenbergite-acmite, with applications to eclogitic rocks. *American Mineralogist*, 92(7), 1181–1189. <https://doi.org/10.2138/am.2007.2401>
- Grevel, C., Schreyer, W., & Grevel, K.-D.-S. (2010). REE distribution, mobilization and fractionation in the coesite-bearing “pyrope quartzite” and related rocks of the Dora-Maira Massif, Western Alps. *European Journal of Mineralogy*, 21(6), 1213–1224. <https://doi.org/10.1127/0935-1221/2009/0021-1967>
- Groppo, C., Beltrando, M., & Compagnoni, R. (2009). The P-T path of the ultra-high pressure Lago Di Cignana and adjoining high-pressure meta-ophiolitic units: Insights into the evolution of the subducting Tethyan slab. *Journal of Metamorphic Geology*, 27(3), 207–231. <https://doi.org/10.1111/j.1525-1314.2009.00814.x>
- Guillong, M., Meier, D. L., Allan, M. M., Heinrich, C. A., & Yardley, B. W. D. (2008). SILLS: A Matlab-based program for the reduction of laser ablation ICP-MS data of homogeneous materials and inclusions. *Mineralogical Association of Canada Short Course*, 40, 328–333.
- Hara, T., Tsujimori, T., Chang, Q., & Kimura, J. I. (2018). In-situ Sr-Pb isotope geochemistry of lawsonite: A new method to investigate slab-fluids. *Lithos*, 320–321, 93–104. <https://doi.org/10.1016/j.lithos.2018.09.001>
- Henk, A., von Blanckenburg, F., Finger, F., Schaltegger, U., & Zulauf, G. (2000). Syn-convergent high-temperature metamorphism and magmatism in the Variscides: A discussion of potential heat sources. *Geological Society Special Publication*, 179, 387–399. <https://doi.org/10.1144/GSL.SP.2000.179.01.23>
- Hertgen, S., Yamato, P., Morales, L. F. G., & Angiboust, S. (2017). Evidence for brittle deformation events at eclogite-facies P-T conditions (example of the Mt. Emilius klippe, Western Alps). *Tectonophysics*, 706–707, 1–13. <https://doi.org/10.1016/j.tecto.2017.03.028>
- Herwartz, D., Nagel, T. J., Münker, C., Scherer, E. E., & Froitzheim, N. (2011). Tracing two orogenic cycles in one eclogite sample by Lu-Hf garnet chronometry. *Nature Geoscience*, 4(3), 178–183. <https://doi.org/10.1038/ngeo1060>
- Holland, T., & Powell, R. (1998). An internally consistent thermodynamic data set for phases of petrological interest. *Journal of Metamorphic Geology*, 16(3), 309–343. <https://doi.org/10.1111/j.1525-1314.1998.00140.x>
- Holland, T., & Powell, R. (2003). Activity-compositions relations for phases in petrological calculations: An asymmetric multicomponent formulation. *Contributions to Mineralogy and Petrology*, 145(4), 492–501. <https://doi.org/10.1007/s00410-003-0464-z>
- Hollister, L. S. (1966). Garnet zoning: An interpretation based on the Rayleigh fractionation model. *Science*, 154(3757), 1647–1651. <https://doi.org/10.1126/science.154.3757.1647>
- Jamtveit, B., & Hervig, R. L. (1994). Constraints on transport and kinetics in constraints on transport hydrothermal systems from zoned garnet crystals. *Science*, 263(5146), 505–508.
- Jochum, K. P., Weis, U., Stoll, B., Kuzmin, D., Yang, Q., Raczek, I., Jacob, D. E., Stracke, A., Birbaum, K., Frick, D. A., Günther, D., & Enzweiler, J. (2011). Determination of reference values for NIST SRM 610–617 glasses following ISO guidelines. *Geostandards and Geoanalytical Research*, 35(4), 397–429. <https://doi.org/10.1111/j.1751-908X.2011.00120.x>
- Jochum, K. P., Willbold, M., Raczek, I., Stoll, B., & Herwig, K. (2005). Chemical characterisation of the USGS reference glasses GSA-1G, GSC-1G, GSD-1G, GSE-1G, BCR-2G, BHVO-2G and BIR-1G Using EPMA, ID-TIMS, ID-ICP-MS and LA-ICP-MS. *Geostandards and Geoanalytical Research*, 29(3), 285–302. <https://doi.org/10.1111/j.1751-908X.2005.tb00901.x>
- Kirst, F., & Leiss, B. (2016). Kinematics of syn- and post-exhumational shear zones at Lago di Cignana (Western Alps, Italy): Constraints on the exhumation of Zermatt-Saas (ultra)high-pressure rocks and deformation along the Combin Fault and Dent Blanche Basal Thrust. *International Journal of Earth Sciences*, 106(1), 215–236. <https://doi.org/10.1007/s00531-016-1316-1>
- Kohn, M. J. (2003). Geochemical zoning in metamorphic mineral. *Treatise on Geochemistry*, 3, 229–261.
- Kohn, M. J. (2009). Models of garnet differential geochronology. *Geochimica et Cosmochimica Acta*, 73(1), 170–182. <https://doi.org/10.1016/j.gca.2008.10.004>
- Kohn, M. J. (2020). A refined zirconium-in-rutile thermometer. *American Mineralogist*, 105, 963–971. <https://doi.org/10.2138/am-2020-7091>
- Konrad-Schmolke, M., Babist, J., Handy, M. R., & O'Brien, P. J. (2006). The physico-chemical properties of a subducted slab from garnet zonation patterns (Sesia Zone, Western Alps). *Journal of Petrology*, 47(11), 2123–2148. <https://doi.org/10.1093/petrology/egl039>
- Konrad-Schmolke, M., Halama, R., Wirth, R., Thomen, A., Klitscher, N., Morales, L., Schreiber, A., & Wilke, F. D. H. (2018). Mineral dissolution and reprecipitation mediated by an amorphous phase. *Nature Communications*, 9(1), 1–9. <https://doi.org/10.1038/s41467-018-03944-z>
- Konrad-Schmolke, M., O'Brien, P. J., de Capitani, C., & Carswell, D. A. (2008). Garnet growth at high- and ultra-high pressure conditions and the effect of element fractionation on mineral modes and composition. *Lithos*, 103(3–4), 309–332. <https://doi.org/10.1016/j.lithos.2007.10.007>
- Konrad-Schmolke, M., Zack, T., O'Brien, P. J., & Barth, M. (2011). Fluid migration above a subducted slab – Thermodynamic and trace element modelling of fluid-rock interaction in partially overprinted eclogite-facies rocks (Sesia Zone, Western Alps). *Earth and Planetary Science Letters*, 311(3–4), 287–298. <https://doi.org/10.1016/j.epsl.2011.09.025>

- Konrad-Schmolke, M., Zack, T., O'Brien, P. J., & Jacob, D. E. (2008). Combined thermodynamic and rare earth element modelling of garnet growth during subduction: Examples from ultrahigh-pressure eclogite of the Western Gneiss Region, Norway. *Earth and Planetary Science Letters*, 272(1–2), 488–498. <https://doi.org/10.1016/j.epsl.2008.05.018>
- Kurz, W., Handler, R., & Bertoldi, C. (2008). Tracing the exhumation of the eclogite zone (Tauern window, Eastern Alps) by <sup>40</sup>Ar/<sup>39</sup>Ar dating of white mica in eclogites. *Swiss Journal of Geosciences*, 101(Suppl. 1), 191–206. <https://doi.org/10.1007/s00015-008-1281-1>
- Kurz, W., Neubauer, F., & Dachs, E. (1998). Eclogite meso- and microfabrics: Implications for the burial and exhumation history of eclogites in the Tauern Window (Eastern Alps) from P-T-d paths. *Tectonophysics*, 285, 183–209. [https://doi.org/10.1016/S0040-1951\(97\)00188-1](https://doi.org/10.1016/S0040-1951(97)00188-1)
- Lagos, M., Scherer, E. E., Tomaschek, F., Münker, C., Keiter, M., Berndt, J., & Ballhaus, C. (2007). High precision Lu-Hf geochronology of Eocene eclogite-facies rocks from Syros, Cyclades, Greece. *Chemical Geology*, 243(1–2), 16–35. <https://doi.org/10.1016/j.chemgeo.2007.04.008>
- Lanari, P. (2012). *Micro-cartographie P-T-e dans les roches métamorphiques. Applications aux Alpes et à l'Himalaya*: Grenoble University.
- Lanari, P., & Duesterhoeft, E. (2019). Modeling metamorphic rocks using equilibrium thermodynamics and internally consistent databases: Past achievements, problems and perspectives. *Journal of Petrology*, 60(1), 19–56. <https://doi.org/10.1093/petrology/egy105>
- Lanari, P., & Engi, M. (2017). Local bulk composition effects on metamorphic mineral assemblages. *Reviews in Mineralogy and Geochemistry*, 83(1), 55–102. <https://doi.org/10.2138/rmg.2017.83.3>
- Lanari, P., Giuntoli, F., Loury, C., Burn, M., & Engi, M. (2017). An inverse modeling approach to obtain P-T conditions of metamorphic stages involving garnet growth and resorption. *European Journal of Mineralogy*, 29(2), 181–199. <https://doi.org/10.1127/ejm/2017/0029-2597>
- Lanari, P., & Piccoli, F. (2020). New horizons in quantitative compositional mapping – Analytical conditions and data reduction using XMapTools. *IOP Conference Series: Materials Science and Engineering*, 891. <https://doi.org/10.1088/1757-899x/891/1/012016>
- Lanari, P., Vho, A., Bovay, T., Airaghi, L., & Centrella, S. (2019). Quantitative compositional mapping of mineral phases by electron probe micro-analyser. *Geological Society Special Publication*, 478(1), 39–63. <https://doi.org/10.1144/SP478.4>
- Lanari, P., Vidal, O., De Andrade, V., Dubacq, B., Lewin, E., Grosch, E. G., & Schwartz, S. (2014). XMapTools: A MATLAB®-based program for electron microprobe X-ray image processing and geothermobarometry. *Computers and Geosciences*, 62, 227–240. <https://doi.org/10.1016/j.cageo.2013.08.010>
- Lapen, T. J., Johnson, C. M., Baumgartner, L. P., Mahlen, N. J., Beard, B. L., & Amato, J. M. (2003). Burial rates during prograde metamorphism of an ultra-high-pressure terrane: An example from Lago di Cignana, western Alps, Italy. *Earth and Planetary Science Letters*, 215(1–2), 57–72. [https://doi.org/10.1016/S0012-821X\(03\)00455-2](https://doi.org/10.1016/S0012-821X(03)00455-2)
- Le Bayon, B., & Ballèvre, M. (2004). Field and petrological evidence for a Late Palaeozoic (Upper Carboniferous-Permian) age of the Erfaulet orthogneiss (Gran Paradiso, western Alps). *Comptes Rendus - Geoscience*, 336(12), 1079–1089. <https://doi.org/10.1016/j.crte.2004.04.004>
- Li, B., Ge, J., & Zhang, B. (2018). Diffusion in garnet: A review. *Acta Geochimica*, 37(1), 19–31. <https://doi.org/10.1007/s11663-017-0187-x>
- Locatelli, M., Verlaquet, A., Agard, P., Federico, L., & Angiboust, S. (2018). Intermediate-depth brecciation along the subduction plate interface (Monviso eclogite, W. Alps). *Lithos*, 320–321, 378–402. <https://doi.org/10.1016/j.lithos.2018.09.028>
- Locatelli, M., Verlaquet, A., Agard, P., Pettke, T., & Federico, L. (2019). Fluid pulses during stepwise Brecciation at intermediate subduction depths (Monviso Eclogites, W. Alps): First internally then externally sourced. *Geochemistry, Geophysics, Geosystems*, 20(11), 5285–5318. <https://doi.org/10.1029/2019GC008549>
- Ludwig, K. R. (2003). Isoplot/Ex version 3.0. A geochronological toolkit for Microsoft Excel. Berkeley Geochronological Centre Special Publications, Berkeley, p. 70.
- Manzotti, P., & Ballèvre, M. (2013). Multistage garnet in high-pressure metasediments: Alpine overgrowths on variscan detrital grains. *Geology*, 41(11), 1151–1154. <https://doi.org/10.1130/G34741.1>
- Manzotti, P., Ballèvre, M., Zucali, M., Robyr, M., & Engi, M. (2014). The tectonometamorphic evolution of the Sesia-Dent Blanche nappes (internal Western Alps): Review and synthesis. *Swiss Journal of Geosciences*, 107(2–3), 309–336. <https://doi.org/10.1007/s00015-014-0172-x>
- Manzotti, P., Rubatto, D., Darling, J., Zucali, M., Cenki-Tok, B., & Engi, M. (2012). From Permo-Triassic lithospheric thinning to Jurassic rifting at the Adriatic margin: Petrological and geochronological record in Valtourneche (Western Italian Alps). *Lithos*, 146–147, 276–292. <https://doi.org/10.1016/j.lithos.2012.05.007>
- Martin, L. A. J., Rubatto, D., Vitale Brovarone, A., & Hermann, J. (2011). Late Eocene lawsonite-eclogite facies metasomatism of a granulite sliver associated to ophiolites in Alpine Corsica. *Lithos*, 125(1–2), 620–640. <https://doi.org/10.1016/j.lithos.2011.03.015>
- Massonne, H. J., & Schreyer, W. (1987). Phengite geobarometry based on the limiting assemblage with K-feldspar, phlogopite, and quartz. *Contributions to Mineralogy and Petrology*, 96(2), 212–224. <https://doi.org/10.1007/BF00375235>
- Messiga, B., & Scambelluri, M. (1991). Retrograde P-T-t path for the Voltri Massif eclogites (Ligurian Alps, Italy): Some tectonic implications. *Journal of Metamorphic Geology*, 9, 93–109. <https://doi.org/10.1111/j.1525-1314.1991.tb00506.x>
- Mibe, K., Yoshino, T., Ono, S., Yasuda, A., & Fujii, T. (2003). Connectivity of aqueous fluid in eclogite and its implications for fluid migration in the Earth's interior. *Journal of Geophysical Research: Solid Earth*, 108(B6), 1–10. <https://doi.org/10.1029/2002j b001960>
- Moore, S. J., Carlson, W. D., & Hesse, M. (2013). Origins of yttrium and rare earth element distributions in metamorphic garnet. *Journal of Metamorphic Geology*, 31(6), 663–689. <https://doi.org/10.1111/jmg.12039>
- Münker, C., Weyer, S., Scherer, E. E., & Mezger, K. (2001). Separation of high field strength elements (Nb, Ta, Zr, Hf) and Lu from rock samples for MC-ICPMS measurements. *Geochemistry, Geophysics, Geosystems*, 2(12). <https://doi.org/10.1029/2001GC000183>
- Negro, F., Bousquet, R., Vils, F., Pellet, C. M., & Hänggi-Schaub, J. (2013). Thermal structure and metamorphic evolution of the Piemont-Ligurian metasediments in the northern Western Alps. *Swiss Journal of Geosciences*, 106(1), 63–78. <https://doi.org/10.1007/s00015-013-0119-7>
- O'Brien, P. J. (2000). The fundamental Variscan problem: High-temperature metamorphism at different depths and high-pressure

- metamorphism at different temperatures. *Orogenic Processes: Quantification and Modelling in the Variscan Belt*, 179(1967), 369–386.
- Okamoto, K., & Maruyama, S. (1999). The high-pressure synthesis of lawsonite in the MORB+H<sub>2</sub>O system. *American Mineralogist*, 84(3), 362–373. <https://doi.org/10.2138/am-1999-0320>
- Otamendi, J. E., de la Rosa, J. D., Patino Douce, A. E., & Castro, A. (2002). Rayleigh fractionation of heavy rare earths and yttrium during metamorphic garnet growth. *Geology*, 30(2), 159–162. [https://doi.org/10.1130/0091-7613\(2002\)030<0159:RFOHR E>2.0.CO;2](https://doi.org/10.1130/0091-7613(2002)030<0159:RFOHR E>2.0.CO;2)
- Paton, C., Hellstrom, J., Paul, B., Woodhead, J., & Hergt, J. (2011). Iolite: Freeware for the visualisation and processing of mass spectrometric data. *Journal of Analytical Atomic Spectrometry*, 26(12), 2508–2518. <https://doi.org/10.1039/c1ja10172b>
- Peacock, S. M., & Wang, K. (1999). Seismic consequences of warm versus cool subduction metamorphism: Examples from southwest and northeast Japan. *Science*, 286(5441), 937–939. <https://doi.org/10.1126/science.286.5441.937>
- Perchuk, A. L., Burchard, M., Schertl, H. P., Maresch, W. V., Gerya, T. V., Bernhardt, H. J., & Vidal, O. (2009). Diffusion of divalent cations in garnet: Multi-couple experiments. *Contributions to Mineralogy and Petrology*, 157(5), 573–592. <https://doi.org/10.1007/s00410-008-0353-6>
- Péron-Pinvidic, G., & Manatschal, G. (2009). The final rifting evolution at deep magma-poor passive margins from Iberia-Newfoundland: A new point of view. *International Journal of Earth Sciences*, 98(7), 1581–1597. <https://doi.org/10.1007/s00531-008-0337-9>
- Peters, D., & Pettke, T. (2017). Evaluation of major to ultra trace element bulk rock chemical analysis of nanoparticulate pressed powder pellets by LA-ICP-MS. *Geostandards and Geoanalytical Research*, 41(1), 5–28. <https://doi.org/10.1111/ggr.12125>
- Pettke, T., Oberli, F., Audétat, A., Guillong, M., Simon, A. C., Hanley, J. J., & Klemm, L. M. (2012). Recent developments in element concentration and isotope ratio analysis of individual fluid inclusions by laser ablation single and multiple collector ICP-MS. *Ore Geology Reviews*, 44, 10–38. <https://doi.org/10.1016/j.oregeorev.2011.11.001>
- Philpotts, A., & Ague, J. J. (2009). *Principles of igneous and metamorphic petrology* (2nd ed). Cambridge University Press.
- Pleuger, J., Roller, S., Walter, J. M., Jansen, E., & Froitzheim, N. (2007). Structural evolution of the contact between two Penninic nappes (Zermatt-Saas zone and Combin zone, Western Alps) and implications for the exhumation mechanism and palaeogeography. *International Journal of Earth Sciences*, 96(2), 229–252. <https://doi.org/10.1007/s00531-006-0106-6>
- Poli, S., & Schmidt, M. W. (2002). Petrology of subducted slabs. *Annual Review of Earth and Planetary Sciences*, 30(1), 207–235. <https://doi.org/10.1146/annurev.earth.30.091201.140550>
- Putnis, A. (2002). Mineral replacement reactions: From macroscopic observations to microscopic mechanisms. *Mineralogical Magazine*, 66(5), 689–708. <https://doi.org/10.1180/0026461026650056>
- Putnis, A. (2009). Mineral replacement reactions. *Reviews in Mineralogy and Geochemistry*, 70, 87–124. <https://doi.org/10.2138/rmg.2009.70.3>
- Raimondo, T., Payne, J., Wade, B., Lanari, P., Clark, C., & Hand, M. (2017). Trace element mapping by LA-ICP-MS: Assessing geochemical mobility in garnet. *Contributions to Mineralogy and Petrology*, 172(4), 1–22. <https://doi.org/10.1007/s00410-017-1339-z>
- Ratschbacher, L., Dingeldey, C., Miller, C., Hacker, B. R., & McWilliams, M. O. (2004). Formation, subduction, and exhumation of Penninic oceanic crust in the Eastern Alps: Time constraints from <sup>40</sup>Ar/<sup>39</sup>Ar geochronology. *Tectonophysics*, 394(3–4), 155–170. <https://doi.org/10.1016/j.tecto.2004.08.003>
- Reinecke, T. (1991). Very high-pressure metamorphism and uplift of coesite-bearing metasediments from the Zermatt-Saas zone, Western Alps. *European Journal of Mineralogy*, 3, 7–17.
- Reinecke, T. (1998). Prograde high- to ultrahigh-pressure metamorphism and exhumation of oceanic sediments at Lago di Cignana, Zermatt-Saas Zone, western Alps. *Lithos*, 42(3–4), 147–189. [https://doi.org/10.1016/s0024-4937\(97\)00041-8](https://doi.org/10.1016/s0024-4937(97)00041-8)
- Rubatto, D., & Angiboust, S. (2015). Oxygen isotope record of oceanic and high-pressure metasomatism: A P-T-time-fluid path for the Monviso eclogites (Italy). *Contributions to Mineralogy and Petrology*, 170(5–6). <https://doi.org/10.1007/s00410-015-1198-4>
- Rubatto, D., Gebauer, D., & Fanning, M. (1998). Jurassic formation and Eocene subduction of the Zermatt-Saas-Fee ophiolites: Implications for the geodynamic evolution of the Central and Western Alps. *Contributions to Mineralogy and Petrology*, 132(3), 269–287. <https://doi.org/10.1007/s004100050421>
- Rubatto, D., & Hermann, J. (2001). Exhumation as fast as subduction? *Geology*, 29(1), 3–6. [https://doi.org/10.1130/0091-7613\(2001\)029<0003:EAFAS>2.0.CO;2](https://doi.org/10.1130/0091-7613(2001)029<0003:EAFAS>2.0.CO;2)
- Rubatto, D., & Hermann, J. (2003). Zircon formation during fluid circulation in eclogites (Monviso, Western Alps): Implications for Zr and Hf budget in subduction zones. *Geochimica et Cosmochimica Acta*, 67(12), 2173–2187. [https://doi.org/10.1016/S0016-7037\(02\)01321-2](https://doi.org/10.1016/S0016-7037(02)01321-2)
- Sandmann, S., Nagel, T. J., Herwartz, D., Fonseca, R. O. C., Kurzwski, R. M., Münker, C., & Froitzheim, N. (2014). Lu–Hf garnet systematics of a polymetamorphic basement unit: New evidence for coherent exhumation of the Adula Nappe (Central Alps) from eclogite-facies conditions. *Contributions to Mineralogy and Petrology*, 168(5), 1–21. <https://doi.org/10.1007/s00410-014-1075-6>
- Scherer, E. E., Cameron, K. L., & Blichert-Toft, J. (2000). Lu–Hf garnet geochronology: Closure temperature relative to the Sm–Nd system and the effects of trace mineral inclusions. *Geochimica et Cosmochimica Acta*, 64(19), 3413–3432. [https://doi.org/10.1016/S0016-7037\(00\)00440-3](https://doi.org/10.1016/S0016-7037(00)00440-3)
- Scherer, E. E., Münker, C., & Mezger, K. (2001). Calibration of the Lutetium–Hafnium Clock. *Science*, 293, 683–688. <https://doi.org/10.1126/science.1061372>
- Sizova, E., Hauzenberger, C., Fritz, H., Faryad, S. W., & Gerya, T. (2019). Late orogenic heating of (Ultra)high pressure rocks: Slab Rollback vs. Slab Breakoff. *Geosciences (Switzerland)*, 9(12), 1–28. <https://doi.org/10.3390/geosciences9120499>
- Skora, S., Baumgartner, L. P., Mahlen, N. J., Johnson, C. M., Pilet, S., & Hellebrand, E. (2006). Diffusion-limited REE uptake by eclogite garnets and its consequences for Lu–Hf and Sm–Nd geochronology. *Contributions to Mineralogy and Petrology*, 152(6), 703–720. <https://doi.org/10.1007/s00410-006-0128-x>
- Skora, S., Mahlen, N. J., Johnson, C. M., Baumgartner, L. P., Lapen, T. J., Beard, B. L., & Szilvagy, E. T. (2015). Evidence for protracted prograde metamorphism followed by rapid exhumation of the Zermatt-Saas Fee ophiolite. *Journal of Metamorphic Geology*, 33(7), 711–734. <https://doi.org/10.1111/jmg.12148>
- Smit, M. A., Scherer, E. E., Bröcker, M., & Van Roermund, H. L. M. (2010). Timing of eclogite facies metamorphism in the southernmost Scandinavian Caledonides by Lu–Hf and Sm–Nd geochronology.

- Contributions to Mineralogy and Petrology*, 159(4), 521–539. <https://doi.org/10.1007/s00410-009-0440-3>
- Smit, M. A., Scherer, E. E., & Mezger, K. (2013). Lu-Hf and Sm-Nd garnet geochronology: Chronometric closure and implications for dating petrological processes. *Earth and Planetary Science Letters*, 381, 222–233. <https://doi.org/10.1016/j.epsl.2013.08.046>
- Söderlund, U., Patchett, P. J., Vervoort, J. D., & Isachsen, C. E. (2004). The  $^{176}\text{Lu}$  decay constant determined by Lu-Hf and U-Pb isotope systematics of Precambrian mafic intrusions. *Earth and Planetary Science Letters*, 219(3–4), 311–324. [https://doi.org/10.1016/S0012-821X\(04\)00012-3](https://doi.org/10.1016/S0012-821X(04)00012-3)
- Spandler, C., Hermann, J., Arculus, R. J., & Mavrogenes, J. (2003). Redistribution of trace elements during prograde metamorphism from lawsonite blueschist to eclogite facies: Implications for deep subduction-zone processes. *Contributions to Mineralogy and Petrology*, 146(2), 205–222. <https://doi.org/10.1007/s00410-003-0495-5>
- Spear, F. S. (1988). Metamorphic fractional crystallization and internal metasomatism by diffusional homogenization of zoned garnets. *Contributions to Mineralogy and Petrology*, 99(4), 507–517. <https://doi.org/10.1007/BF00371941>
- Spear, F. S. (2017). Garnet growth after overstepping. *Chemical Geology*, 466, 491–499. <https://doi.org/10.1016/j.chemgeo.2017.06.038>
- Spear, F. S., & Pattison, D. R. M. (2017). The implications of overstepping for metamorphic assemblage diagrams (MADs). *Chemical Geology*, 457, 38–46. <https://doi.org/10.1016/j.chemgeo.2017.03.011>
- Spear, F. S., & Wolfe, O. M. (2019). Implications of overstepping of garnet nucleation for geothermometry, geobarometry and P-T path calculations. *Chemical Geology*, 530. <https://doi.org/10.1016/j.chemgeo.2019.119323>
- Taylor, S. R., & McLennan, S. M. (1985). *The continental crust: Its composition and evolution*. Blackwell Scientific Publications.
- Thiessen, E. J., Gibson, H. D., Regis, D., Pehrsson, S. J., Cutts, J. A., & Smit, M. A. (2019). High-grade metamorphism flying under the radar of accessory minerals. *Geology*, 47(6), 568–572. <https://doi.org/10.1130/G45979.1>
- Usui, T., Kobayashi, K., Nakamura, E., & Helmstaedt, H. (2007). Trace element fractionation in deep subduction zones inferred from a lawsonite-eclogite xenolith from the Colorado Plateau. *Chemical Geology*, 239(3–4), 336–351. <https://doi.org/10.1016/j.chemgeo.2006.08.009>
- Vance, D., & Onions, R. K. (1990). Isotopic chronometry of zoned garnets: Growth kinetics and metamorphic histories. *Earth and Planetary Science Letters*, 97(3–4), 227–240. [https://doi.org/10.1016/0012-821X\(90\)90044-X](https://doi.org/10.1016/0012-821X(90)90044-X)
- Vitale Brovarone, A., Alard, O., Beyssac, O., Martin, L., & Picatto, M. (2014). Lawsonite metasomatism and trace element recycling in subduction zones. *Journal of Metamorphic Geology*, 32(5), 489–514. <https://doi.org/10.1111/jmg.12074>
- Vitale Brovarone, A., Beltrando, M., Malavieille, J., Giuntoli, F., Tondella, E., Groppo, C., Beyssac, O., & Compagnoni, R. (2011). Inherited ocean-continent transition zones in deeply subducted terranes: Insights from Alpine Corsica. *Lithos*, 124(3–4), 273–290. <https://doi.org/10.1016/j.lithos.2011.02.013>
- Vitale Brovarone, A., & Beyssac, O. (2014). Lawsonite metasomatism: A new route for water to the deep Earth. *Earth and Planetary Science Letters*, 393, 275–284. <https://doi.org/10.1016/j.epsl.2014.03.001>
- Vogt, K., & Gerya, T. V. (2014). From oceanic plateaus to allochthonous terranes: Numerical modelling. *Gondwana Research*, 25(2), 494–508. <https://doi.org/10.1016/j.gr.2012.11.002>
- Walsh, E. O., & Hacker, B. R. (2004). The fate of subducted continental margins: Two-stage exhumation of the high-pressure to ultrahigh-pressure Western Gneiss Region, Norway. *Journal of Metamorphic Geology*, 22(7), 671–687. <https://doi.org/10.1111/j.1525-1314.2004.00541.x>
- Weber, S., & Bucher, K. (2015). An eclogite-bearing continental tectonic slice in the Zermatt-Saas high-pressure ophiolites at Trockener Steg (Zermatt, Swiss Western Alps). *Lithos*, 232, 336–359. <https://doi.org/10.1016/j.lithos.2015.07.010>
- Weber, S., Sandmann, S., Miladinova, I., Fonseca, R. O. C., Froitzheim, N., Munker, C., & Bucher, K. (2015). Dating the initiation of Piemonte-Liguria ocean subduction: Lu-Hf garnet chronometry of eclogites from the Theodul Glacier Unit (Zermatt-Saas zone, Switzerland). *Swiss Journal of Geosciences*, 108(2–3), 183–199. <https://doi.org/10.1007/s00015-015-0180-5>
- White, R. W., Powell, R., & Holland, T. J. B. (2007). Progress relating to calculation of partial melting equilibria for metapelites. *Journal of Metamorphic Geology*, 25(5), 511–527. <https://doi.org/10.1111/j.1525-1314.2007.00711.x>
- White, R. W., Powell, R., Holland, T. J. B., & Worley, B. (2000). The effect of  $\text{TiO}_2$  and  $\text{Fe}_2\text{O}_3$  on metapelitic assemblages at greenschist and amphibolite facies conditions: Mineral equilibria calculations in the system  $\text{K}_2\text{O}-\text{FeO}-\text{MgO}-\text{Al}_2\text{O}_3-\text{SiO}_2-\text{H}_2\text{O}-\text{TiO}_2-\text{Fe}_2\text{O}_3$ . *Journal of Metamorphic Geology*, 18(5), 497–511. <https://doi.org/10.1046/j.1525-1314.2000.00269.x>
- Whitney, D. L., & Evans, B. W. (2010). Abbreviations for names of rock-forming minerals. *American Mineralogist*, 95(1), 185–187. <https://doi.org/10.2138/am.2010.3371>
- Whitney, D. L., Teyssier, C., Toraman, E., Seaton, N. C. A., & Fayon, A. K. (2011). Metamorphic and tectonic evolution of a structurally continuous blueschist-to-Barrovian terrane, Sivrihisar Massif, Turkey. *Journal of Metamorphic Geology*, 29(2), 193–212. <https://doi.org/10.1111/j.1525-1314.2010.00915.x>
- Wiederkehr, M., Bousquet, R., Schmid, S. M., & Berger, A. (2008). From subduction to collision: Thermal overprint of HP/LT meta-sediments in the north-eastern Lepontine Dome (Swiss Alps) and consequences regarding the tectono-metamorphic evolution of the Alpine orogenic wedge. *Swiss Journal of Geosciences*, 101(suppl. 1). <https://doi.org/10.1007/s00015-008-1289-6>
- Wilke, F. D. H., O'Brien, P. J., Altenberger, U., Konrad-Schmolke, M., & Khan, M. A. (2010). Multi-stage reaction history in different eclogite types from the Pakistan Himalaya and implications for exhumation processes. *Lithos*, 114(1–2), 70–85. <https://doi.org/10.1016/j.lithos.2009.07.015>
- Wolfe, O. M., & Spear, F. S. (2018). Determining the amount of overstepping required to nucleate garnet during Barrovian regional metamorphism, Connecticut Valley Synclinorium. *Journal of Metamorphic Geology*, 36(1), 79–94. <https://doi.org/10.1111/jmg.12284>

## SUPPORTING INFORMATION

Additional supporting information may be found online in the Supporting Information section.

**Figure S1.** Quantified LA-ICP-MS compositional maps in garnet, all maps show  $\mu\text{g/g}$  abundance.

**Figure S2.** Quantified LA-ICP-MS compositional maps in

garnet, all maps show  $\mu\text{g/g}$  abundance.

**Figure S3.** Quantified LA-ICP-MS compositional maps in garnet, all maps show  $\mu\text{g/g}$  abundance.

**Figure S4.** BSE image of garnet.

**Figure S5.** EPMA profile across chloritoid grains.

**Figure S6.** Ternary chemical diagram showing the range of garnet composition in  $X_{\text{grs}}-X_{\text{alm}}-X_{\text{prp}}$ .

**Figure S7.** Pseudosection of sample Z16TB11 with garnet  $\text{Grt}_{\text{MS},1}$   $P-T$  stable condition.

**Figure S8.** Pseudosection of sample Z16TB11 with garnet  $\text{Grt}_{\text{MS},2}$   $P-T$  stable condition.

**Figure S9.** Pseudosection of sample Z16TB11 with garnet  $\text{Grt}_{\text{MS},3}$   $P-T$  stable condition.

**Figure S10.** Pictures of garnet separates for Lu-Hf dating.

**Figure S11.**  $P-T$  diagrams presenting variation of  $\text{H}_2\text{O}$  in solids with superimposed pseudosections.

**Figure S12.** Outcrop pictures and scanned thin section images illustrating fluid-rock interaction in TGU.

**Table S1.** Garnet major element average composition.

**Table S2.** LA-ICP-MS trace element of garnet.

**Table S3.** K-white mica major element average composition.

**Table S4.** Chloritoid major element chemical composition.

**Table S5.** LA-ICP-MS trace element of rutile.

**Table S6.** Reactive bulk rock chemistry evolution using GrtMode.

**Table S7.** LA-ICP-MS major and trace element bulk rock analyses.

**How to cite this article:** Bovay, T., Lanari, P., Rubatto, D., Smit, M., & Piccoli, F. (2022). Pressure-temperature-time evolution of subducted crust revealed by complex garnet zoning (Theodul Glacier Unit, Switzerland). *Journal of Metamorphic Geology*, 40(2), 175–206. <https://doi.org/10.1111/jmg.12623>